Depletion of *Mettl3* in cholinergic neurons causes adult-onset neuromuscular degeneration

Graphical abstract

Highlights

- *Mettl3* depletion in cholinergic neurons causes an adult-onset neuromuscular phenotype

- Motor neurons are selectively affected by *Mettl3* depletion

- m⁶A profiling reveals extensive modification of TARDBP

- m⁶A methylation is required for TDP-43 autoregulation

Authors

Georgia Dermentzaki, Mattia Furlan, Iris Tanaka, ..., Dario Bonanomi, Mattia Pelizzola, Francesco Lotti

Correspondence

fl2219@cumc.columbia.edu

In brief

Dermentzaki et al. report that *Mettl3* depletion in cholinergic neurons results in a progressive decline in motor behaviors, accompanied by selective motor neuron loss and muscle denervation, culminating in paralysis and death at around 8 months of age. m⁶A profiling reveals modification of TARDBP and extensive regulation of its expression.
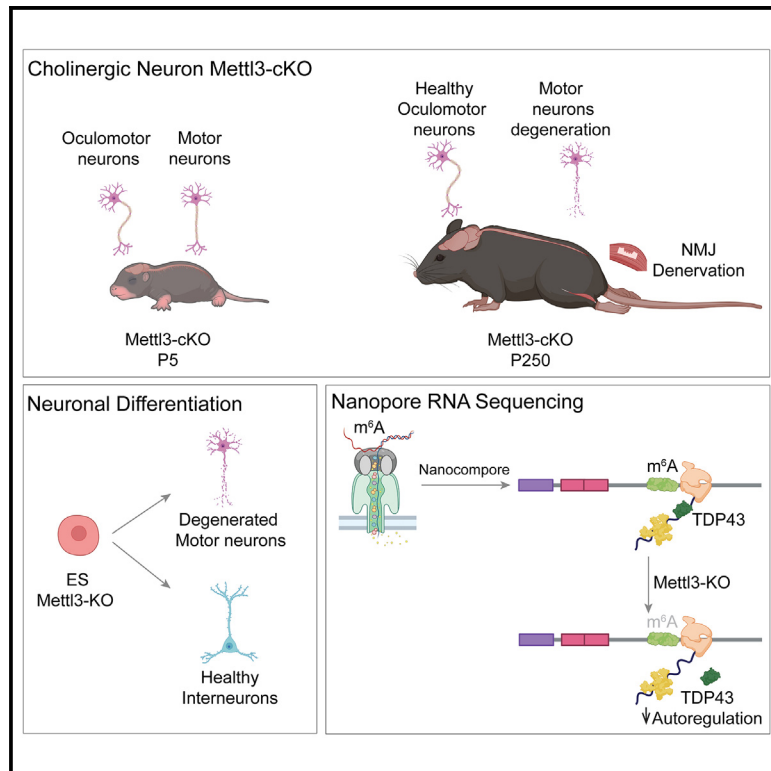
CelPress

Report

Depletion of *Mettl3* in cholinergic neurons causes adult-onset neuromuscular degeneration

Georgia Dermentzaki,[1] Mattia Furlan,[2] Iris Tanaka,[2] Tommaso Leonardi,[2] Paola Rinchetti,[1] Patricia M.S. Passos,[3] Alliny Bastos,[3] Yuna M. Ayala,[3] Jacob H. Hanna,[4] Serge Przedborski,[1,5] Dario Bonanomi,[6] Mattia Pelizzola,[2,7] and Francesco Lotti[1,8,*]

[1]Center for Motor Neuron Biology and Disease, Departments of Pathology & Cell Biology and Neurology, Columbia University, New York, NY, USA
[2]Center for Genomic Science of IIT@SEMM, Fondazione Istituto Italiano di Tecnologia, Milan, Italy
[3]Department of Biochemistry & Molecular Biology, St. Louis University School of Medicine, St. Louis, Missouri, USA
[4]Department of Molecular Genetics, Weizmann Institute of Science, Rehovot, Israel
[5]Department of Neuroscience, Columbia University, New York, NY, USA
[6]Division of Neuroscience, IRCCS San Raffaele Scientific Institute, Milan, Italy
[7]Department of Biotechnology and Biosciences, University of Milano-Bicocca, Milan, Italy
[8]Lead contact
*Correspondence: fl2219@cumc.columbia.edu
https://doi.org/10.1016/j.celrep.2024.113999

SUMMARY

Motor neuron (MN) demise is a hallmark of several neurodegenerative diseases, including amyotrophic lateral sclerosis (ALS). Post-transcriptional gene regulation can control RNA's fate, and defects in RNA processing are critical determinants of MN degeneration. N^6-methyladenosine (m^6A) is a post-transcriptional RNA modification that controls diverse aspects of RNA metabolism. To assess the m^6A requirement in MNs, we depleted the m^6A methyltransferase-like 3 (METTL3) in cells and mice. METTL3 depletion in embryonic stem cell-derived MNs has profound and selective effects on survival and neurite outgrowth. Mice with cholinergic neuron-specific METTL3 depletion display a progressive decline in motor behavior, accompanied by MN loss and muscle denervation, culminating in paralysis and death. Reader proteins convey m^6A effects, and their silencing phenocopies METTL3 depletion. Among the m^6A targets, we identified transactive response DNA-binding protein 43 (TDP-43) and discovered that its expression is under epitranscriptomic control. Thus, impaired m^6A signaling disrupts MN homeostasis and triggers neurodegeneration conceivably through TDP-43 deregulation.

INTRODUCTION

Spinal motor neurons (MNs) are the key mediators translating motor commands generated within the central nervous system (CNS) to peripheral skeletal muscles. MNs cannot regenerate, and the mechanisms that govern their maintenance in the adult CNS are essential for proper motor functions and survival. Mounting evidence indicates that both cell-autonomous and non-cell-autonomous signaling pathways recruit intrinsic neuronal signaling cascades,[1] which, upon integration and processing, form an interconnected molecular network essential for cell survival and circuit maintenance.[2] Adding to the complexity of this crucial molecular network is the fact that its composition and regulation may vary in different cell types and biological settings. This is consistent with the well-known differential susceptibility of MNs to pathological situations where, even in response to ubiquitous insults, hypoglossal and spinal MNs that control the ability to speak, breathe, and move are among the first to die. In contrast, the oculomotor and Onuf's MNs that control vision and sexual and bladder

function are relatively spared.[3] Marked differences in vulnerability are also evident among MN pools located in the same spinal cord region, with fast motor units degenerating before slow motor units.[4–6]

Little is known about the properties and modulation of the intrinsic molecular network that defines subtype-specific responses of MNs to cell-autonomous and non-cell-autonomous signals. Several genes mutated in MN diseases function at different steps of the mRNA life cycle.[7] In addition to mutation, RNA metabolism can be altered by the cellular aggregates containing RNA-binding proteins, such as transactive response DNA-binding protein 43 (TDP-43). TDP-43 is not only pivotal for post-transcriptional gene regulation but is also critically involved in age-related neurodegeneration.[8] For instance, aggregated TDP-43 has been found in almost all cases of ALS and approximately 45% of patients with frontotemporal dementia (FTD).[9] Similarly, TDP-43 abnormalities have also been observed in up to 57% of Alzheimer's disease (AD) cases and many cases of Parkinson's disease, revealing the breadth of disorders characterized by TDP-43 pathology.[10,11] The current

view is that the levels and subcellular localization of TDP-43 must be tightly controlled to ensure its function.[12] An aberrant increase of TDP-43 levels results in neurotoxicity as observed in human neurons[13] and in a wide range of animal models.[14–19] TDP-43 levels are kept under tight control through an autoregulatory mechanism in which TDP-43 binds to its mRNA and reduces its protein output.[20,21] Disruption of this autoregulatory mechanism in mouse models results in widespread splicing changes, neurotoxicity,[19,22,23] and increased cytoplasmic TDP-43 aggregation.[24,25] Given the increasingly recognized relevance of RNA metabolism in MN biology, here we set out to resolve the contribution of epigenetic RNA modification—specifically, N^6-methyladenosine (m^{6}A)—to MN physiology and differential vulnerability.

RNA modifications are chemical changes introduced post-transcriptionally to enable rapid fine-tuning of gene expression in response to specific contextual cues. Among more than 160 known RNA modifications, m^{6}A is the most abundant in the CNS.[26–28] m^{6}A is installed by a methyltransferase "writer" complex whose core catalytic element is the methyltransferase-like 3 (METTL3). m^{6}A is strongly enriched in the DRACH consensus motif (D = A, G, or U; H = A, C, or U) and occurs preferentially near stop codons and 5′ and 3′ UTRs.[27,29] m^{6}A can be reversed by demethylases that function as "erasers" (e.g., fat mass and obesity-associated protein [FTO]). The effects of m^{6}A on RNA metabolism and gene expression are mediated by RNA binding proteins (RBPs) termed "readers" that recognize and decode the m^{6}A mark, ultimately conveying a plethora of downstream events, including pre-mRNA splicing, nuclear export, stability, and translation. Proteins containing the YT521-B homology (YTH) domain, including cytoplasmic YTH domain family 1–3 (YTHDF1–YTHDF3) and nuclear YTH domain containing 1–2 (YTHDC1–YTHDC2) in mammals, bind directly to methylated RNA.[30] Instead, other readers, such as heterogeneous nuclear ribonucleoproteins (hnRNPs), fragile X mental retardation protein (FMRP), and insulin growth factor 2 mRNA-binding proteins 1–3 (IGF2BP1–IGF2BP3) utilize common RNA binding domains to bind m^{6}A-containing RNAs.[31]

Consistent with the enrichment of m^{6}A in the CNS[26,28] and its widespread effects on gene expression, deregulation of this modification affects RNA processing events that underlie neurological diseases.[32,33] Whole-genome sequencing has revealed an association between *FTO* gene variants and sporadic ALS cases,[34] and ALS-linked mutations have been identified in the m^{6}A reader hnRNPA2B1.[35] In addition, TLS/FUS (translocated in liposarcoma/fused in sarcoma) has been reported to function as an m^{6}A reader, and transfection of cells with m^{6}A-modified RNA fragments dissolves stress-induced cytoplasmic FUS foci, enhancing cell viability.[36] While these studies highlight the impact of m^{6}A on motor system physiology, the effects and regulation of m^{6}A signaling in MNs are unknown. To address this question, we generated mouse mutants lacking METTL3 in spinal MNs. We established MN cultures from *Mettl3* knockout (KO) embryonic stem cells (ESCs), which predictably showed a dramatic reduction in m^{6}A levels. Surprisingly, we found that METTL3 was dispensable for MN development and the assembly of neuromuscular connectivity. Instead, *Mettl3* mutants displayed an adult-onset, progressive ALS-like phenotype characterized by loss of fast-fatigable MNs, muscle denervation, impaired motor control, paralysis, and death. Nanopore-based direct RNA sequencing revealed changes in m^{6}A in transcripts that operate in molecular processes required for MN survival and function. Among these m^{6}A targets, we found *TARDBP*, the transcript coding for TDP-43, and discovered that its expression is under epitranscriptomic regulation. Overall, our findings establish m^{6}A as a critical determinant of MN homeostasis and link the loss of this mark on *TARDBP* to altered self-regulation of TDP-43 expression, which might instigate neurodegeneration.

RESULTS

Depletion of *Mettl3* in cholinergic neurons results in an adult-onset neuromuscular phenotype

To study the role of m^{6}A signaling in MNs, we sought to delete *Mettl3* in mice, since the lack of this core methyltransferase leads to substantial depletion of m^{6}A marks.[37] *Mettl3* is an essential gene, and homozygous deletion causes lethality at an early embryonic stage.[38] To overcome germline lethality and inactivate the m^{6}A pathway, specifically in MNs, we combined a conditional allele of *Mettl3* that contains *loxP* sites flanking exon 4,[39] with *ChAT-Cre*, which expresses Cre recombinase under the control of the choline acetyltransferase (ChAT) promoter active in spinal MNs after embryonic day 12.5.[40,41] Efficient conditional KO (cKO) was confirmed by selective depletion of METTL3 in the nucleus of ChAT-positive cells, as revealed by immunostaining of the spinal cord (Figure 1A). In addition, spinal cord immunostaining with antibodies recognizing m^{6}A on the RNA confirms that *Mettl3* cKO in cholinergic neurons strongly reduced m^{6}A levels in MNs (Figure S1A). *Mettl3* cKO mice were born with the expected Mendelian ratios and developed normally until post-natal day 100 (P100), when the body weight reached a plateau and then started to decrease after P150 in both male and female mutant mice (Figures 1B and 1C). By the end stage (P250), mutant mice presented with ~30% less body mass and severe muscle wasting (Figure S1B). Symptoms worsened with age, and the animals reached an endpoint (the righting reflex exceeding 30″) around 8 months of age, with no difference between sexes (median: 275 male, 281 female; Figures 1D and 1E).

Since *Mettl3*-cKO mice presented with progressive muscle wasting and weakness, we performed behavioral tests to characterize their neuromuscular phenotype. Starting at P50, we assessed their motor performance with a grip strength test (inverted grid). We found that *Mettl3* cKO mice exhibited a deficit in muscle strength by ~P90 and progressively worsened as they reached the end stage (Figure 1F). Motor coordination, balance, and endurance, assessed with the rotarod test, progressively declined in *Mettl3* cKO mice after P150 (Figure 1G). The impairment in motor behavior was comparable in mutant males and females (Figures S1C and S1D).

We then performed the open field test to assess general motor function and exploratory activity starting at P90. The traveled distance and time spent in the center of the arena during this task were similar between control and *Mettl3*-cKO mice at P90 and P150 (Figure S1E), while both parameters were severely affected in mutants at P210 (Figures 1H and 1I).
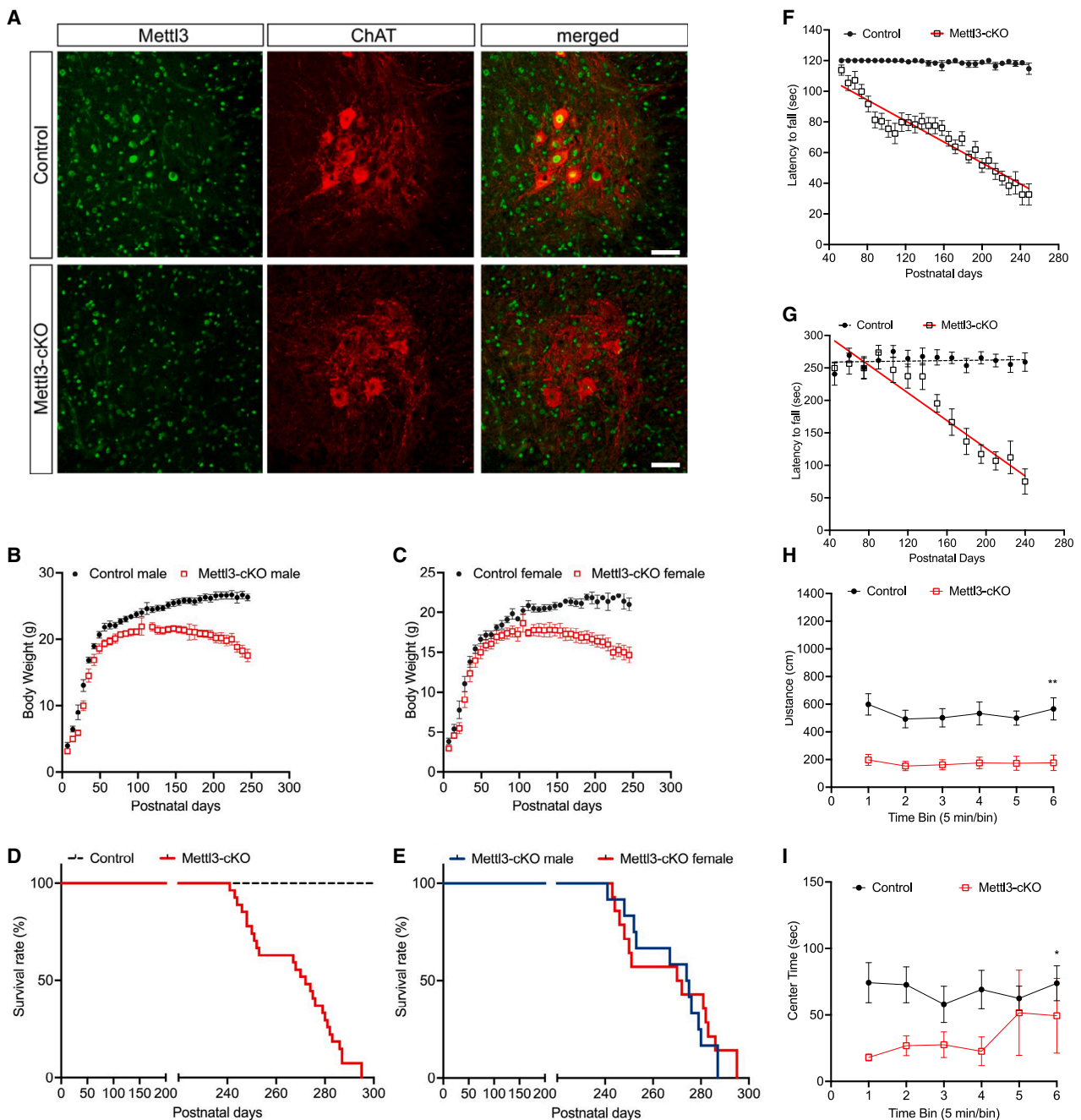
Figure 1. Depletion of *Mettl3* in cholinergic neurons results in an adult-onset neuromuscular phenotype

(A) Spinal cords from 2-week-old control and *Mettl3* cKO mice were stained with anti-METTL3 (green) and anti-ChAT (red) antibodies. Scale bars, 25 μM.

(B and C) Progressive loss of body weight (grams) in male (n = 6–8/genotype) and female (n = 6–8/genotype) *Mettl3* cKO mice.

(D and E) Kaplan-Meier survival curve for *Mettl3* cKO mice. Log rank (Mantel-Cox) test (p < 0.0001); median all mice: 272, n = 27; median male: 274.5, n = 12; median female: 271, n = 15.

(F) Inverted grid (n = 21–25/genotype).

(G) Rotarod (n = 12–13/genotype).

(F and G) Data were analyzed by a non-linear regression curve fit using the least sum-of-squares method (p < 0.0001).

(H) Open field: ambulatory distance (centimeters) (n = 9–10/genotype, 7 months). There is a significant main effect of genotype ($F_{1,16}$ = 26.776, p < 0.001).

(I) Open field: center time (seconds) (n = 9–10/genotype, 7 months). There is a significant main effect of genotype ($F_{1,16}$ = 5.250, p = 0.036).

(H and I) Data were analyzed by two-way repeated measures ANOVA.

All data in (B), (C), and (F)–(I) are means ± SEM.

See also Figure S1.
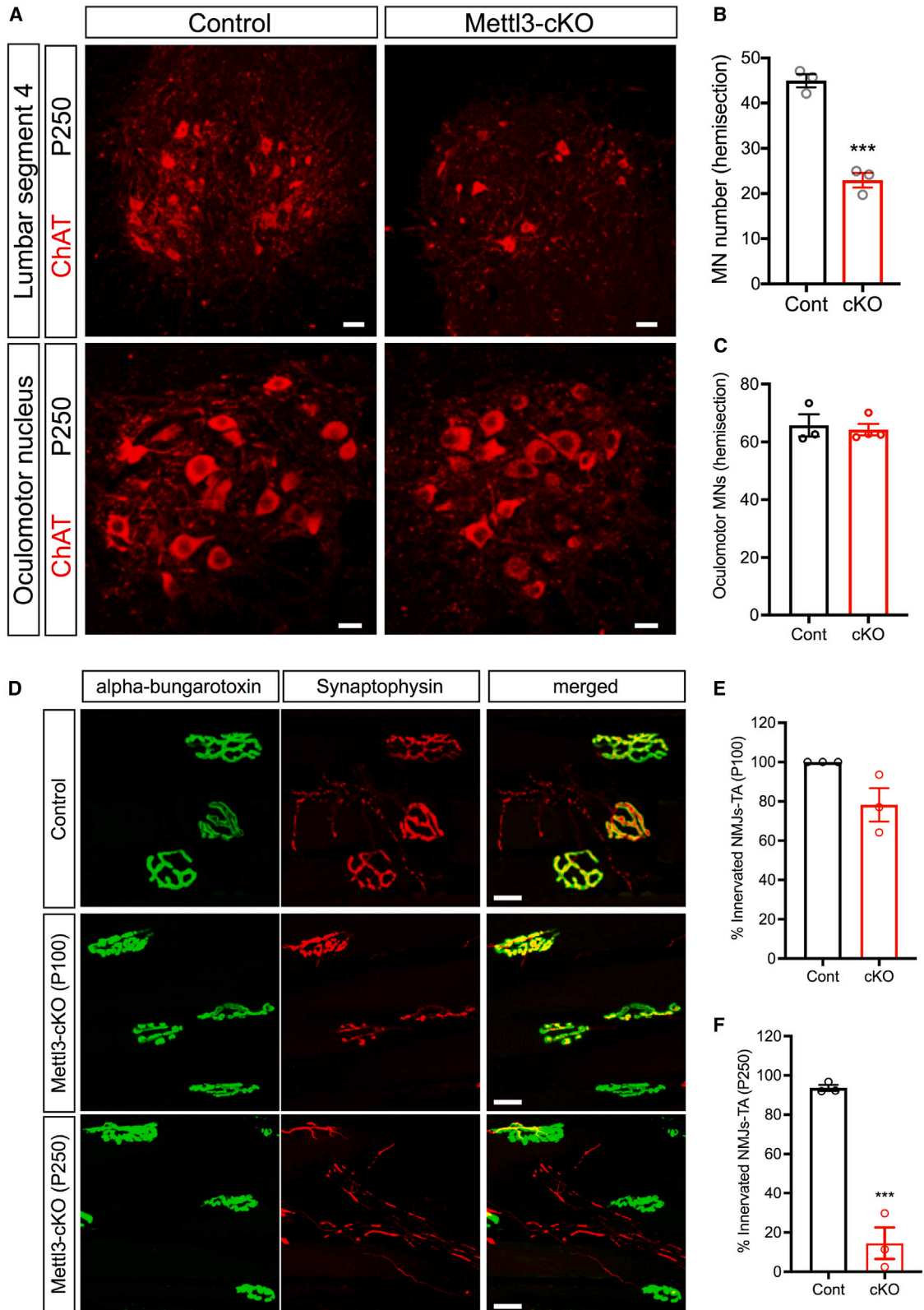
(legend on next page)

MNs are differentially affected by METTL3 depletion

Given our findings of a faster decline in strength and shortened lifespan of *Mettl3* cKO mice, we sought to determine the effect of m6A loss on MN survival. Therefore, we counted the number of MNs present in the lumbar 4 and 5 (L4-L5) segments of the spinal cord at P5 (pre-symptomatic), P100 (early symptomatic), and P250 (end stage). We found that MN numbers in the *Mettl3* cKO mice were similar to the control at P5 and P100 (Figures S2A–S2C) but were markedly reduced (~50%) at P250 (Figures 2A and 2B). Of note, astrogliosis was already evident at P100 (Figure S2A), indicating that the process of MN degeneration had already started, although the number of MNs was not altered at this stage.

While robust loss of MNs was detected at the end stage in the L4-L5 region, ~50% of MNs were still present (Figures 2A and 2B). This incomplete penetrance prompted us to examine the density of MNs in other spinal cord segments to assess whether MNs displayed differential susceptibility to m6A loss. Strikingly, we found that MNs innervating oculomotor muscles in the brain stem were resistant to *Mettl3* depletion (Figures 2A and 2C). This situation matches the pattern of differential vulnerability observed in adult-onset MN diseases such as ALS, where MNs innervating fast fatigable (FF) muscle fibers exhibit enhanced susceptibility compared with those innervating slow resistant (S) muscle fibers.[3] Matrix metallopeptidase 9 (MMP9) is a recognized marker of FF-innervating MNs and, consequently, labels vulnerable MNs in mouse models of ALS.[42,43] We found that ~80% of MMP9+ MNs were lost in the L4 segment in end-stage *Mettl3* cKO mice (Figures S2D and S2E). This observation was corroborated by analysis of motor endplate innervation in the *tibialis anterior* (TA) muscle, mainly composed of FF fibers.[44] Overlap of the presynaptic marker synaptophysin (red) and the postsynaptic marker α-bungarotoxin (green) revealed that TA neuromuscular junctions (NMJs) were severely denervated at the end stage in *Mettl3* cKO mice (P250), with signs of denervation already evident at P100 (Figures 2D–2F).

METTL3 depletion results in the selective degeneration of ESC-MNs

The severe phenotype detected in *Mettl3* cKO mice prompted us to elucidate the pathways affected in MNs due to METTL3 depletion and, by extension, m6A loss. To this end, we utilized CRISPR-Cas9 editing to target the endogenous *Mettl3* locus in mouse ESCs and generated truncated out-of-frame alleles by deleting exon 4 (Figure S3A). Complete loss of METTL3 was confirmed by western blot (Figure S3B). *Mettl3*−/− ESCs retained normal morphology and proliferation rate (Figure S3C). ESCs can be efficiently differentiated into spinal MNs following a well-established protocol that gives rise to a population of postmitotic

neurons in which ~30% are MNs (ESC-MNs), and the remainder are spinal interneurons (ESC-INs).[45,46] Since ESCs used for these assays express GFP under the control of the MN-specific promoter Hb9,[47] the efficiency of MN differentiation can be determined by quantification of GFP-expressing cells by flow cytometry (fluorescence-activated cell sorting [FACS]). FACS analysis of wild-type (WT) and KO ESC-MNs revealed that *Mettl3* ablation impaired MN differentiation compared with the control (Figures S3D and S3E).

To determine the effect of *Mettl3* depletion on neuronal survival and neurite length, we FACS-sorted equal numbers of control and *Mettl3* KO ESC-MNs based on GFP expression and cultured them in 96-well plates.[47,48] In parallel, we collected GFP-negative ESC-INs from the same differentiated ESCs to assess the impact of *Mettl3* ablation in these cells. Cell numbers and neurite length measurements in individual neurons were obtained through automated high-content imaging of fluorescently labeled axons and cell bodies (Figure 3A).[48] Using this system, we found that *Mettl3* depletion decreased ESC-MN survival and neurite outgrowth (Figures 3A–3C). Similar results were observed by lentiviral vector (LV)-mediated knockdown of *Mettl3* in ES-MNs after differentiation, suggesting that the observed degeneration is not the result of a deficit in differentiation (Figures S3F3G and 3H). Importantly, neither process was affected in *Mettl3* KO ESC-INs (Figures 3D–3F), indicating that ESC-MNs are particularly susceptible to m6A loss.

The selective impairment observed in ESC-MNs prompted us to study how m6A signaling is regulated in MNs and the consequences of its loss on mRNA homeostasis. First, to determine whether ESC-MN degeneration was the result of impaired METTL3 methyltransferase activity, we used LVs to express WT or catalytically compromised METTL3 (METTL3-APPA; DPPW motif mutated to APPA[49]) in *Mettl3*-KO ESC-MNs. Remarkably, while expression of METTL3 WT corrected the phenotype of *Mettl3* KO ESC-MNs, expression of METTL3-APPA did not, suggesting that METTL3 methyltransferase function is required for MN survival (Figures S3G–S3J).

Then, to investigate whether the effects of *Mettl3* ablation on ESC-MNs were reader-dependent, we used an LV to silence the YTHDF family of readers.[50,51] After differentiation, ESC-MNs were dissociated, plated in 96-well plates, and cultured for 3 days before transduction with LVs expressing short hairpin RNA (shRNA) targeting *Ythdf1-3* (Figure S3F). Control cultures were treated with an LV expressing the scrambled shRNA sequence (Figure S3F). Knockdown of *Ythdf1* or *Ythdf3* led to robust MN loss and reduced neurite outgrowth after 8 days in culture compared with the control (Figures 3I, 3J, 3M, and 3N), whereas knockdown of *Ythdf2* did not have a significant effect (Figures 3K and 3L). These results suggest that, in the context

Figure 2. MNs are differentially affected by *Mettl3* depletion

(A) Representative images of ChAT immunostaining in ventral lumbar segments 4 and 5 (L4-L5) of the spinal cord and oculomotor MNs in the brain stem from control and *Mettl3* cKO mice at the end stage (P250). Scale bars, 50 μm.

(B and C) Quantification of (B) MN number per hemi-section (p = 0.0006) and (C) oculomotor MNs (p = 0.7227).

(D) Immunostaining of synaptophysin (red) and α-bungarotoxin (green) in the *tibialis anterior* (TA) from control and *Mettl3* cKO mice at P100 and P250. Scale bars, 10μM.

(E and F) Quantification of neuromuscular junction (NMJ) innervation status at (E) P100, (p = 0.0628) and (F) P250 (p < 0.0001).

Data are means ± SEM of n = 3–4 independent experiments analyzed by unpaired t test. See also Figure S2.
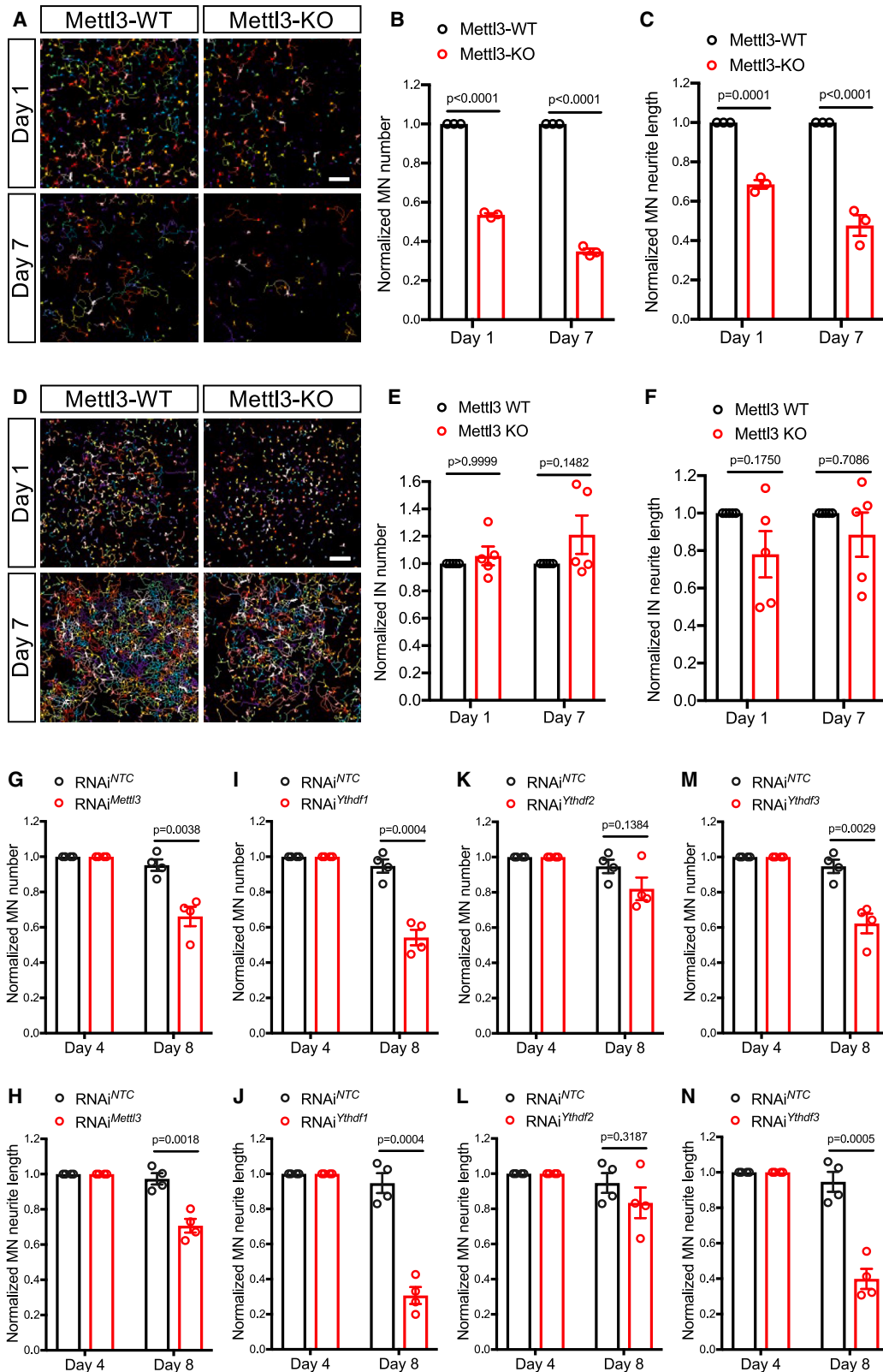
(legend on next page)

of ESC-MNs, YTHDF readers might have distinct roles (and mRNA targets) rather than functioning redundantly to control mRNA decay, as suggested previously for cancer cell lines.[52]

Next, we sought to determine whether YTHDF2 was involved in the ESC-MN degeneration elicited by *Mettl3* KO, as this m⁶A reader has been reported recently to modulate the survival of neurons carrying ALS-associated mutations.[53] Therefore, we performed a rescue experiment using an LV expressing YTHDF2 and found that the expression of this reader had a minimal impact on the phenotype of *Mettl3* KO ESC MNs (Figures S3G–S3J).

Nanopore-based direct RNA sequencing identifies *TARDBP* as an m⁶A target

To investigate the link between m⁶A loss and MN demise, we determined the m⁶A landscape of ESC-MNs and the relative changes in gene expression downstream of METTL3 depletion. To this end, we used Nanopore-based direct RNA sequencing (DRS),[54] which does not require retro-transcription and amplification steps and, therefore, preserves transcript modifications, enabling their detection through their footprints on intensity signals.[55] With DRS, we sought to identify m⁶A sites lost following METTL3 depletion by directly comparing ESC-MNs differentiated from WT and *Mettl3* KO ESCs.[56] mRNA was prepared from 2 biological replicates of FACS-sorted ESC-MNs and, together with a technical replicate for each condition, was sequenced with the GridION Nanopore platform. The sequencing yielded an average of 2.9e6 reads per sample with an average length of 631 bp (Figure S4A).[54] Highly expressed genes were strongly enriched in Gene Ontology terms associated with neuronal functions (Figure S4B). Hierarchical clustering of gene expression data indicated a good separation between WT and *Mettl3* KO samples and a high correlation between biological and technical replicates (Figures S4C and S4D), confirming the quality of DRS data.

To identify m⁶A sites, we used the Gaussian mixture model implemented in Nanocompore[56] to compare the ionic-current intensity and dwell times between WT and *Mettl3* KO conditions for 4,034 genes with high coverage. Since the ionic-current signal in DRS is detected at the level of 5-mers starting at each base of the transcript sequence, the identified m⁶A sites match differences in signal at specific 5-mers. Using *Mettl3* KO samples as a baseline, we identified 5,486 significant m⁶A sites distributed among 2,023 transcripts and 1,777 genes (Table S1). We examined how methylated sites were distributed along the transcripts and confirmed the expected enrichment around stop codons and 3′ UTRs (Figure 4A). We observed that 96% of the significant sites contained at least one A, and 58% of them matched the known DRACH motif compared

with 74% and 2% for the background, respectively (Figures 4B and 4C). In particular, the GGAC motif was over-represented among these sites, confirming the validity of the identified m⁶A sites (Figure S4E).

Differential gene expression analysis identified 296 upregulated and 650 downregulated genes in *Mettl3* KO cells. Of these, 203 (69%) and 245 (38%) were marked by m⁶A. The enrichment of m⁶A among upregulated genes is consistent with the known role of m⁶A in promoting mRNA decay. *Tardbp* emerged as one of the most prominent m⁶A-modified genes upregulated in *Mettl3*-KO cells, both in terms of the number and significance of m⁶A sites (Figure 4D). *Tardbp* methylation was supported by seven highly significant 5-mers covering five distinct m⁶A sites. These sites have a high methylation rate with stoichiometry ranging from 38% to 72% (Figure 4E). We determined the occurrence of these m⁶A sites within each of the DRS reads spanning this region, together with the corresponding modification probability (Figure 4F). This analysis revealed that each *Tardbp* transcript was often modified at multiple sites. As expected, a similar analysis performed under the *Mettl3* KO condition revealed a prevalence of low modification probabilities (Figures S4F and S4I). In addition, the co-occurrence of m⁶A modifications often involved site 2, suggesting its prominent role as a METTL3 target in *Tardbp* (Figure 4G and Figure S4G). Finally, 622 TDP-43 target genes were expressed at a high level in WT cells (Figure S4H) and were enriched in genes encoding for m⁶A-containing transcripts. 110 targets were differentially expressed in *Mettl3* KO cells, although not in a prevalent direction (50 up- and 60 downregulated). To delve deeper into these differentially expressed TDP-43 targets, we generated a heatmap depicting their fold change, and we annotated each gene with the number of m⁶A sites, their maximum significance, and their mean absolute expression between WT and KO conditions. We observed a stronger methylation signal for upregulated genes (Figure S4J).

Loss of m⁶A impairs TDP-43 autoregulation

Given that all five m⁶A sites identified on *Tardbp* reside within the TDP-43 binding region (TDPBR) of the 3′ UTR to which TDP-43 binds to mediate its autoregulation (Figure 5A), it is plausible that loss of m⁶A marks on *Tardbp* could affect this control mechanism. As a first step, we sought to confirm whether METTL3 depletion results in *Tardbp* m⁶A loss. We quantitatively assessed the levels of m⁶A in *Tardbp* and *Hprt* (an m⁶A-negative transcript) using m⁶A RNA immunoprecipitation (RIP) coupled with RT-qPCR.[57,58] Consistent with DRS data, we found that METTL3 depletion reduced the amount of *Tardbp* RNA recovered in the immunoprecipitation (IP) to background levels (Figure 5B).

Next, we directly assessed whether *Mettl3* knockdown resulted in the loss of TDP-43 autoregulation in human cells. First,

---

Figure 3. METTL3 depletion results in the selective degeneration of ESC-MNs

(A and D) Fields of GFP-expressing ESC-MNs (A) and Tuj1-expressing ESC-INs (D). False colors are assigned to individual neurons by MetaMorph. Scale bars, 200 μm.

(B, C, E, and F) Quantification of (B) MNs (day 1 and day 7, p < 0.0001), (C) MN neurite outgrowth (day 1, p = 0.0001; day 7, p < 0.0001), (E) INs (day 1, p > 0.9999; day 7, p = 0.1482), and (F) IN neurite outgrowth (day 1, p = 0.1750; day 7, p = 0.7086).

(G–N) Quantification of MNs and MN neurite outgrowth, respectively, for *Mettl3* (G, day 8, p = 0.038; H, day 8, p = 0.018), *Ythdf1* (I, day 8, p = 0.0004; J, day 8, p = 0.0004), *Ythdf2* (K, day 8, p = 0.1384; L, day 8, p = 0.3187), and *Ythdf3* (M, day 8, p = 0.0029; N, day 8, p = 0.0005).

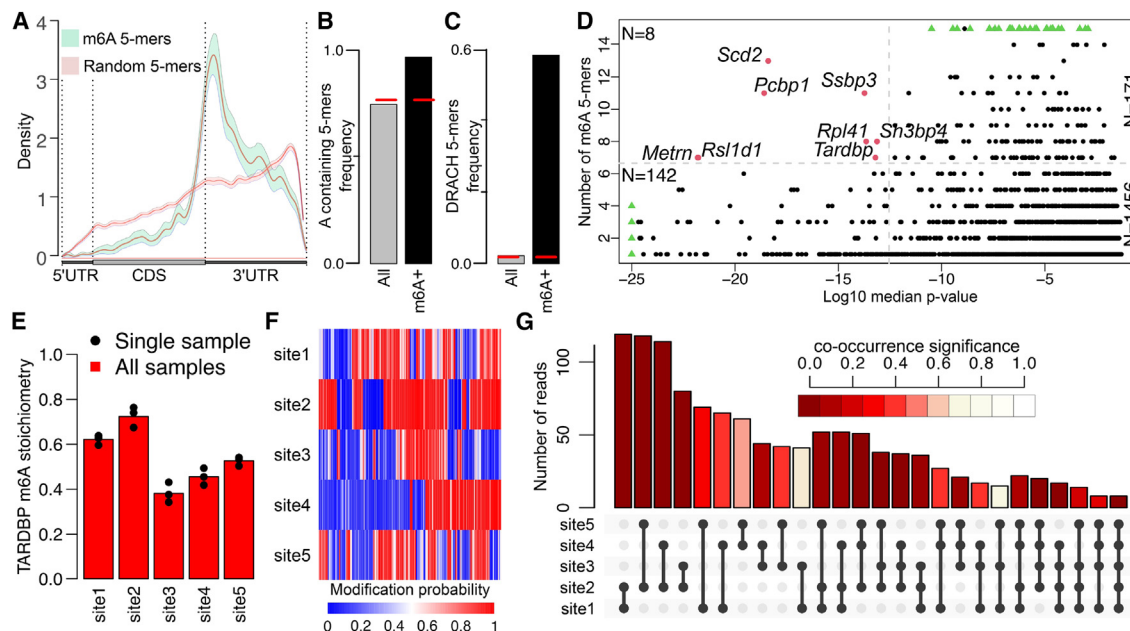Data are means ± SEM of 3 or more independent experiments analyzed by unpaired t test. See also Figure S3.

Figure 4. Nanopore-based DRS identifies _TARDBP_ as an m⁶A target

(A) Metagene distribution of m⁶A+ (green) and randomly selected (red) 5-mers, including 0.95 confidence intervals (shadow).

(B) Frequency of A-containing m⁶A+ 5-mers (black) and any A-containing tested 5-mers (gray). The red dashed line represents the expected frequency for 5-mers composed of 5 nt randomly extracted with a probability of 0.25.

(C) As in (B) for DRACH 5-mers.

(D) Scatterplot reporting the numbers and median significance of identified m⁶A+ 5-mers (generalized method of moments logit-adjusted p < 0.05) for each of the 1,777 genes coding m⁶A+ transcripts. Shown in red are 8 top-ranking genes for the number and significance of m⁶A 5-mers (thresholds set at 95% of the _TARDBP_ values, gray dashed lines). Green triangles identify genes saturated at the axis maximum values.

(E) Stoichiometry of the 5 m⁶A sites detected on _TARDBP_.

(F) Heatmap showing the WT modification probability for each of the 5 _TARDBP_ m⁶A sites (rows) in each read (columns).

(G) Number of _TARDBP_ reads simultaneously modified in the indicated combinations of 2, 3, 4, and 5 m⁶A sites. The co-occurrence significance reports the number of times the co-occurrence exceeds a null model obtained by shuffling 1,000 times the probabilities of each site.

See also Figure S4 and Table S1.

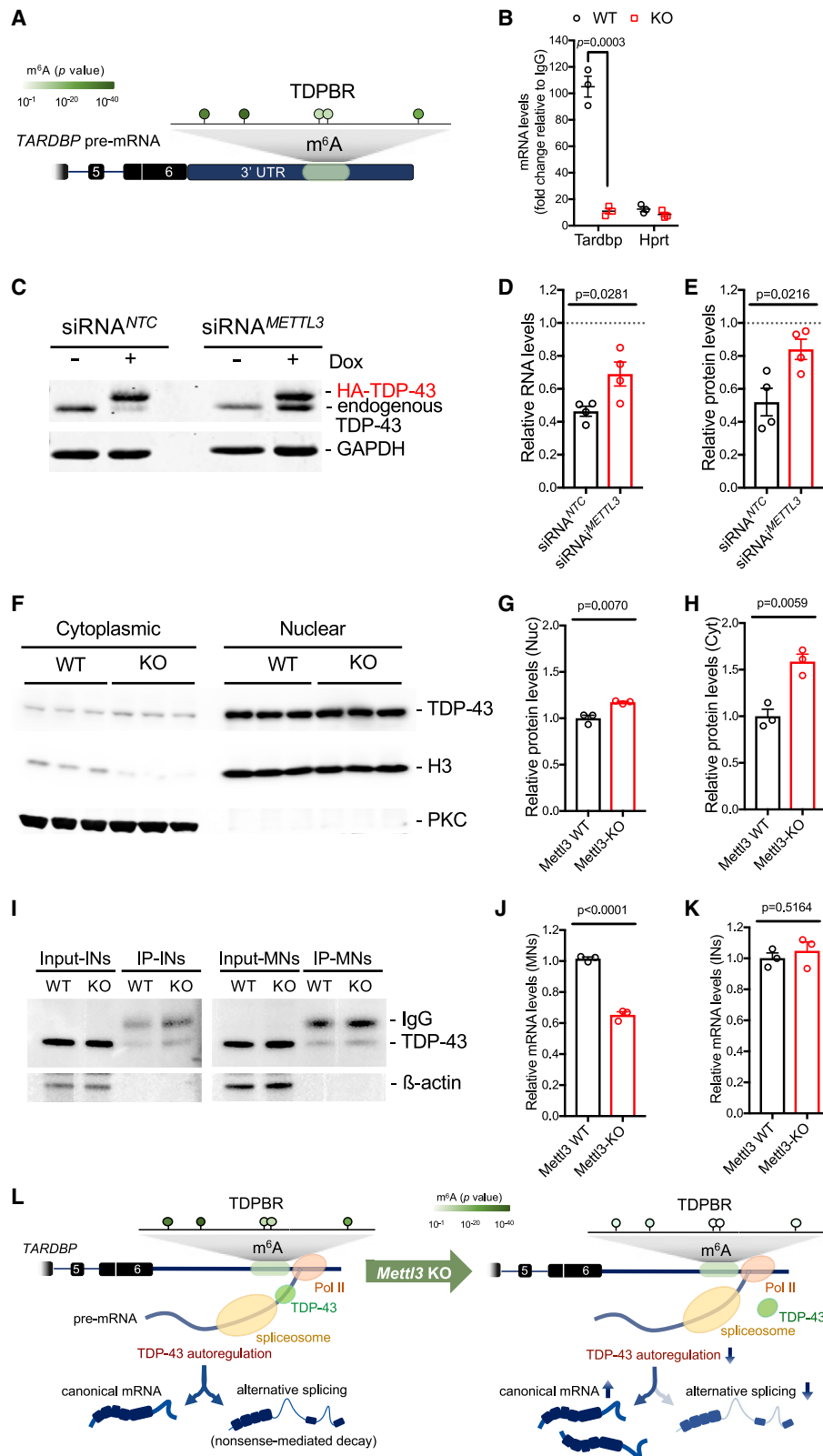we compared the 3′ UTR of mouse and human _TARDBP_. We found that the consensus sequence of all five m⁶A sites is fully conserved (Figure S5A). Then, we used human embryonic kidney cells (HEK293^HA-TDP-43) cells that stably express a single copy of the hemagglutinin (HA)-tagged TDP-43 transgene upon doxycycline (Dox) induction.[59] Expression of HA-TDP-43 results in downregulation of endogenous TDP-43 levels in this cell line. To determine the effect of m⁶A loss on this autoregulatory activity, we silenced _METTL3_ via RNAi and measured endogenous TDP-43 expression 48 h after HA-TDP-43 induction. Cells transfected with _METTL3_ small interfering RNA (siRNA; siRNA^METTL3) displayed a ∼50% reduction in METTL3 expression compared with the non-targeting siRNA control (siRNA^NTC) (Figure S5B). Endogenous TDP-43 RNA and protein levels decreased by ∼50% upon induction of the TDP-43 transgene in siRNA^NTC-transfected cells (Figures 5C–5E). In contrast, when _METTL3_ was silenced in doxycycline-treated cells, endogenous TDP-43 downregulation was attenuated, resulting in an increase in TDP-43 levels in siRNA^METTL3-transfected cells relative to siRNA^NTC-transfected cells (Figures 5D and 5E), while this difference is less evident in untreated cells (Figure S5C).

Afterward, we asked whether TDP-43 autoregulation is impaired in _Mettl3_-KO ESC-MNs. First, we compared endogenous TDP-43

transcript levels in WT versus _Mettl3_ KO ESC-MNs and found that TDP-43 RNA levels were increased in _Mett3_ KO ESC MNs (Figure S5D). Then, we compared TDP-43 protein levels and subcellular distribution, performing nucleo-cytoplasm fractionation of WT and _Mettl3_ KO ESC-MNs, and measured TDP-43 by western blot (Figure 5F). Remarkably, we found that TDP-43 is increased in both compartments of _Mett3_ KO ESC-MNs, with a more pronounced increase in the cytoplasmic fraction, suggesting an accumulation of TDP-43 in this compartment upon METTL3 depletion (Figures 5F–5H).

Next, based on our observation that silencing of _Ythdf1/3_ resulted in ESC-MN degeneration, while _Ythdf2_ did not have any significant effects (Figures 3I–3N), we asked about the impact of knockdown of these readers on _Tardbp_ mRNA levels. Notably, while _Ythdf1_ silencing caused an increase in _Tardbp_ mRNA levels, knockdown of _Ythdf2_ did not (Figure S5E), further suggesting a correlation between ESC-MNs degeneration and altered TDP-43 expression.

One of the determinants of TDP-43 autoregulation is the interaction between TDP-43 and its transcript. To determine whether loss of m⁶A influences this interaction, we performed cross-linking and IP (CLIP) with anti-TDP-43 antibody followed by RT-qPCR to monitor the binding efficiency of TDP-43 to its

A

m⁶A (*p* value)
10^{-1} 10^{-20} 10^{-40}

TDPBR

TARDBP pre-mRNA

m⁶A

5   6   3' UTR

B

○ WT   □ KO

p=0.0003

mRNA levels
(fold change relative to IgG)

Tardbp   Hprt

C

siRNA^NTC   siRNA^METTL3

− + − +   Dox

HA-TDP-43
endogenous TDP-43

GAPDH

D

p=0.0281

Relative RNA levels

siRNA^NTC   siRNA^METTL3

E

p=0.0216

Relative protein levels

siRNA^NTC   siRNA^METTL3

F

Cytoplasmic   Nuclear

WT   KO   WT   KO

TDP-43

H3

PKC

G

p=0.0070

Relative protein levels (Nuc)

Mettl3 WT   Mettl3-KO

H

p=0.0059

Relative protein levels (Cyt)

Mettl3 WT   Mettl3-KO

I

Input-INs   IP-INs   Input-MNs   IP-MNs

WT KO WT KO   WT KO WT KO

IgG
TDP-43

ß-actin

J

p<0.0001

Relative mRNA levels (MNs)

Mettl3 WT   Mettl3-KO

K

p=0.5164

Relative mRNA levels (INs)

Mettl3 WT   Mettl3-KO

L

TDPBR

m⁶A (*p* value)
10^{-1} 10^{-20} 10^{-40}

TDPBR

TARDBP

5   6

m⁶A

Pol II

pre-mRNA

spliceosome

TDP-43

TDP-43 autoregulation

canonical mRNA

alternative splicing

(nonsense-mediated decay)

***Mettl3* KO** →

TARDBP

5   6

m⁶A

Pol II

TDP-43

spliceosome

TDP-43 autoregulation ↓

canonical mRNA ↑

alternative splicing ↓

(legend on next page)

transcript. Differentiated embryoid bodies were UV cross-linked, and then MNs and INs were purified by FACS. Total cell extracts from both neuronal types were prepared and immunoprecipitated with anti-TDP-43 antibody. Western blot analysis showed equal amounts of TDP-43 immunoprecipitated in both WT and *Mettl3* KO cells (Figure 5I). Importantly, RT-qPCR showed a reduced level of TDP-43 transcript immunoprecipitated in *Mettl3* KO ESC-MNs, while ESC-INs were unaffected (Figures 5J and 5K).

Based on these observations, we propose a model where the loss of m[6]A marks on *TARDBP* disrupts TDP-43 binding to its transcript and impairs its autoregulation, which may trigger the cascade of events that culminates with the demise of specific neuronal subtypes caused by abnormally elevated TDP-43 expression (Figure 5L).

DISCUSSION

Spinal MNs are essential for coordinating muscle activity and various voluntary movements. They are also the cellular targets responsible for the progressive and ultimately fatal symptoms of spinal muscular atrophy (SMA) and ALS. A prominent and enigmatic feature of these neurodegenerative diseases is their selective neuronal and regional vulnerability while the pathology-associated proteins are ubiquitously expressed.[60,61] The intrinsic molecular networks behind this differential susceptibility in disease are poorly defined. Here, we used cell-specific depletion of METTL3 to erase m[6]A signatures from differentiated MNs and test this epigenetic RNA modification's contribution to developing and maintaining the spinal motor system.

Deletion of *Mettl3* in cholinergic neurons did not interfere with the embryonic and postnatal development of MNs, since mutant mice were essentially indistinguishable from controls until 3 months of age, and no MN loss was observed during this period. This was surprising, since cKO of either *Mettl3* or *Mettl14* in the embryonic mouse brain has been associated with severe differentiation defects, and we found that *in vitro* derivation of MNs from *Mettl* KO ESCs was inefficient. Deletion of *Mettl3* or *Mettl14* with pan-neuronal *Nestin*::CRE prolonged the cell cycle

of radial glial cells and extended cortical neurogenesis disrupting the development of the cortex and cerebellum,[62,63] whereas *Mettl14* cKO in oligodendrocyte precursor cells (OPCs) with *Olig2*::CRE led to reduced oligodendrocyte numbers and CNS hypomyelination.[64] Of note, *Olig2*::CRE is also active in MN progenitors, but *Mettl14* deletion did not alter MN numbers in the lumbar spinal cord at P12,[64] in line with our findings that m[6]A is required for maintenance rather than the development of the spinal motor system. Overall, these results indicate that the regulatory effects of m[6]A and, by extension, of m[6]A-marked RNA targets are spatially and temporally restricted. Accordingly, profiling of the mouse brain revealed specific regional and temporal m[6]A patterns, which showed biphasic peaks in young and aged mice.[26,65] Time dependency is particularly relevant, since, in our model, *Mettl3* was excised at embryonic day 12.5 (E12.5) after postmitotic specification of MNs rather than in progenitor cells as in previous studies.[62–64] Therefore, m[6]A appears to have a general role in early neuronal and glial cell differentiation. Still, it is dispensable for the establishment of neuromuscular connectivity, implying that the conserved sequence of postmitotic MN development involving motor pool formation, axon pathfinding, and muscle-specific targeting[66–68] does not require m[6]A. In contrast, homeostasis of the spinal motor system critically depends on m[6]A-dependent control of gene expression. Importantly, this requirement is not shared by all MN subtypes but mirrors the pattern of the vulnerability reported in ALS, in which MNs innervating FF muscle fibers are prone to degeneration. Enhanced susceptibility to METTL3 loss was also detected in ESC cultures, where MNs, but not INs, displayed differentiation defects.

Nanopore-based DRS confirmed the pervasive impact of *Mettl3* KO on the m[6]A epitranscriptome, involving the significant reduction of the mark in 5,486 sites distributed among 2,023 transcripts. These data revealed that *Tardbp* is heavily modified by m[6]A in MNs; likewise, TDP-43 targets are enriched in m[6]A marks. We found five distinct m[6]A sites residing in the TDP-43 binding region of *Tardbp* that were also conserved in humans. Loss of m[6]A resulted in impaired TDP-43 autoregulation, suggesting that altered expression of TDP-43 contributes to *Mettl3*

Figure 5. Loss of m[6]A impairs TDP-43 autoregulation

(A) TDP-43 binds to the TDP-43 binding region (TDPBR in green) in the 3′ UTR (blue) of *TARDBP* pre-mRNA. Exons are depicted as boxes, highlighting coding regions (black), and introns as lines.

(B) m[6]A-RIP and RT-qPCR for *Tardpb* in ESC-MNs. The graph depicts the depletion of *Tardpb* in *Mettl3* KO conditions (relative to immunoglobulin G (IgG)). *Hprt* is used as a negative control. Data are means ± SEM of 3 independent experiments analyzed by unpaired t test (p = 0.0003).

(C) Western blot of endogenous TDP-43 levels from doxycycline (Dox)-induced and non-induced HEK293T cells transfected with siRNA[NTC] or siRNA[METTL3]. GAPDH was used as a loading control.

(D and E) Quantification of endogenous *TARDBP* mRNA (D) and TDP-43 protein (E) expression in RNAi-transfected cells with induction (+Dox) of HA-TDP-43 expression relative to non-induced cells (−Dox, dotted line). Data are means ± SEM of 4 independent experiments analyzed by unpaired t test (D, p = 0.4055; E, p = 0.0207).

(F) Western blot of mouse TDP-43 levels in the cytoplasmic or nuclear fraction of *Mettl3* WT and *Mettl3* KO ESC-MN lysates. Histone H3 and protein kinase C (PKC) were used as nuclear or cytoplasmic loading controls, respectively.

(G and H) Quantification of TDP-43 protein levels in nuclear (G) or cytoplasmic (H) fractions from (F). Data are means ± SEM of 3 independent experiments analyzed by unpaired t test (G, p = 0.0070; H, p = 0.0059).

(I) Western blot of mouse TDP-43 levels after IP of TDP-43 in total cell lysates from ESC-INs or ESC-MNs differentiated from *Mettl3* WT or *Mettl3* KO. β-Actin was used as a loading control.

(J and K) Quantification of TDP-43 protein levels in ESC-MNs (J) or ESC-Ins (K) from (I). Data are means ± SEM of 3 independent experiments analyzed by unpaired t test (J, p < 0.0001; K, p = 0.5164).

(L) Model by which the loss of m[6]A marks on *TARDBP* disrupts the interaction between TDP-43 and its transcript and impairs autoregulation.

See also Figure S5.

KO ESC-MN demise. Supporting our findings, a recent study has shown that m⁶A RNA methylation modulates TDP-43 binding and autoregulation.[53] Emphasizing the significance of m⁶A-dependent TDP-43 regulation in ALS, extensive m⁶A hypermethylation was detected in postmortem samples from sporadic ALS patients.[53] Conversely, our study showed that m⁶A depletion, and therefore hypomethylation, was associated with an adult-onset neuromuscular phenotype. Thus, altered m⁶A homeostasis in either direction (hyper- or hypomethylation) triggers MN dysfunction. In support of this scenario, a recent paper showed that global m⁶A hypomethylation in C9ORF72-ALS/FTD dysregulates RNA metabolism and contributes to neurodegeneration.[69] Interestingly, in both mouse and human brains, m⁶A sites were significantly increased in aging and were associated with genes implicated in aging-related pathways.[65] In contrast, m⁶A modification decreased in AD mouse models and correlated with reduced levels of proteins involved in disease pathways.[65] Therefore, the alteration in the m⁶A levels of specific transcripts linked to neurodegenerative diseases, especially in aged individuals, could represent a mechanism that drives adult-onset selective neurodegeneration.

Another degree of selectivity was observed at the level of m⁶A readers. YTHDF1 and YTHDF3 were implicated in MN survival and neurite outgrowth, while YTHDF2 was dispensable. Unlike in MNs, m⁶A readers functioned redundantly in other cell types,[52] pointing to cell-type specificity and possibly task specificity in this regulatory layer. The m⁶A reader-dependent effect on MNs revealed in our work agrees with recent findings showing that TDP-43-related neuronal toxicity is enhanced by *Ythdf1* and *Ythdf3* KO and suppressed by *Ythdf2* KO.[53] These results point to YTHDF2 as a potent genetic modifier of TDP43-mediated toxicity and suggest that identifying downstream RNA targets regulated by YTHDF2 in MNs may open additional therapeutic avenues.

Limitations of the study

Our epitranscriptomic analysis revealed several targets besides TDP-43, including targets relevant to neurodegenerative states. While neglecting these potential attractive candidates, this study deliberately focused on TDP-43 for its relevance to MN degeneration and age-related disorders. Another limitation of the study is the lack of a clear cause-effect relationship between the loss of m⁶A marks on *TARDBP* and *Mettl3* KO ESC-MN degeneration. Future studies may focus on determining the contribution of each m⁶A site to TDP-43 regulation and its link to TDP-43 proteinopathies.

STAR★METHODS

Detailed methods are provided in the online version of this paper and include the following:

- KEY RESOURCES TABLE
- RESOURCE AVAILABILITY
  - Lead contact
  - Materials availability
  - Data and code availability
- EXPERIMENTAL MODEL AND STUDY PARTICIPANT DETAILS
  - Animals
  - Mouse embryonic stem cells (mESCs) cultures
- METHOD DETAILS
  - mESCs differentiation into MNs and lentiviral transduction
  - METTL3 downregulation and TDP-43 autoregulation
  - CRISPR-Cas9 mediated Mettl3 knock-out in Hb9:eGFP ES cells
  - RNA extraction-cDNA synthesis-qPCR
  - m⁶A MeRIP
  - Profiling the m⁶A epitranscriptome
  - Additional bioinformatic analyses
  - Western blotting
  - Immunocytochemistry and immunohistochemistry
  - Mouse behavioral tests
- QUANTIFICATION AND STATISTICAL ANALYSIS

AUTHOR CONTRIBUTIONS

F.L. designed and supervised the study. G.D. designed and performed experiments and analyzed data. P.M.S.P. and A.B. performed experiments. M.F. and T.L. performed computational analyses for the transcriptional and epitranscriptional profiling. I.T. performed the Nanopore sequencing. Y.A., J.H.H., S.P., D.B., and M.P. contributed to data design, analysis, revision, and interpretation. G.D., M.F., Y.A., D.B., M.P., and F.L. wrote the paper with input from all authors.

DECLARATION OF INTERESTS

F.L. is a co-founder and president of a startup company working on antisense oligonucleotide therapeutics.

REFERENCES

1. Kristiansen, M., and Ham, J. (2014). Programmed cell death during neuronal development: the sympathetic neuron model. Cell Death Differ. *21*, 1025–1035. https://doi.org/10.1038/cdd.2014.47.

2. Pfisterer, U., and Khodosevich, K. (2017). Neuronal survival in the brain: neuron type-specific mechanisms. Cell Death Dis. *8*, e2643. https://doi.org/10.1038/cddis.2017.64.

3. Kanning, K.C., Kaplan, A., and Henderson, C.E. (2010). Motor neuron diversity in development and disease. Annu. Rev. Neurosci. *33*, 409–440. https://doi.org/10.1146/annurev.neuro.051508.135722.

4. Frey, D., Schneider, C., Xu, L., Borg, J., Spooren, W., and Caroni, P. (2000). Early and selective loss of neuromuscular synapse subtypes with low sprouting competence in motoneuron diseases. J. Neurosci. *20*, 2534–2542. https://doi.org/10.1523/JNEUROSCI.20-07-02534.2000.

5. Pun, S., Santos, A.F., Saxena, S., Xu, L., and Caroni, P. (2006). Selective vulnerability and pruning of phasic motoneuron axons in motoneuron disease alleviated by CNTF. Nat. Neurosci. *9*, 408–419. https://doi.org/10.1038/nn1653.

6. Spiller, K.J., Cheung, C.J., Restrepo, C.R., Kwong, L.K., Stieber, A.M., Trojanowski, J.Q., and Lee, V.M.Y. (2016). Selective Motor Neuron Resistance and Recovery in a New Inducible Mouse Model of TDP-43 Proteinopathy. J. Neurosci. *36*, 7707–7717. https://doi.org/10.1523/JNEUROSCI.1457-16.2016.

7. Nussbacher, J.K., Tabet, R., Yeo, G.W., and Lagier-Tourenne, C. (2019). Disruption of RNA Metabolism in Neurological Diseases and Emerging Therapeutic Interventions. Neuron *102*, 294–320. https://doi.org/10.1016/j.neuron.2019.03.014.

8. de Boer, E.M.J., Orie, V.K., Williams, T., Baker, M.R., De Oliveira, H.M., Polvikoski, T., Silsby, M., Menon, P., van den Bos, M., Halliday, G.M., et al. (2020). TDP-43 proteinopathies: a new wave of neurodegenerative diseases. J. Neurol. Neurosurg. Psychiatry *92*, 86–95. https://doi.org/10.1136/jnnp-2020-322983.

9. Suk, T.R., and Rousseaux, M.W.C. (2020). The role of TDP-43 mislocalization in amyotrophic lateral sclerosis. Mol. Neurodegener. *15*, 45. https://doi.org/10.1186/s13024-020-00397-1.

10. Cook, C., Zhang, Y.J., Xu, Y.F., Dickson, D.W., and Petrucelli, L. (2008). TDP-43 in neurodegenerative disorders. Expet Opin. Biol. Ther. *8*, 969–978. https://doi.org/10.1517/14712598.8.7.969.

11. Tremblay, C., St-Amour, I., Schneider, J., Bennett, D.A., and Calon, F. (2011). Accumulation of transactive response DNA binding protein 43 in mild cognitive impairment and Alzheimer disease. J. Neuropathol. Exp. Neurol. *70*, 788–798. https://doi.org/10.1097/NEN.0b013e31822c62cf.

12. Tziortzouda, P., Van Den Bosch, L., and Hirth, F. (2021). Triad of TDP43 control in neurodegeneration: autoregulation, localization and aggregation. Nat. Rev. Neurosci. *22*, 197–208. https://doi.org/10.1038/s41583-021-00431-1.

13. Barmada, S.J., Skibinski, G., Korb, E., Rao, E.J., Wu, J.Y., and Finkbeiner, S. (2010). Cytoplasmic mislocalization of TDP-43 is toxic to neurons and enhanced by a mutation associated with familial amyotrophic lateral sclerosis. J. Neurosci. *30*, 639–649. https://doi.org/10.1523/JNEUROSCI.4988-09.2010.

14. Diaper, D.C., Adachi, Y., Sutcliffe, B., Humphrey, D.M., Elliott, C.J.H., Stepto, A., Ludlow, Z.N., Vanden Broeck, L., Callaerts, P., Dermaut, B., et al. (2013). Loss and gain of Drosophila TDP-43 impair synaptic efficacy and motor control leading to age-related neurodegeneration by loss-of-function phenotypes. Hum. Mol. Genet. *22*, 1539–1557. https://doi.org/10.1093/hmg/ddt005.

15. Estes, P.S., Boehringer, A., Zwick, R., Tang, J.E., Grigsby, B., and Zarnescu, D.C. (2011). Wild-type and A315T mutant TDP-43 exert differential neurotoxicity in a Drosophila model of ALS. Hum. Mol. Genet. *20*, 2308–2321. https://doi.org/10.1093/hmg/ddr124.

16. Tatom, J.B., Wang, D.B., Dayton, R.D., Skalli, O., Hutton, M.L., Dickson, D.W., and Klein, R.L. (2009). Mimicking aspects of frontotemporal lobar degeneration and Lou Gehrig's disease in rats via TDP-43 overexpression. Mol. Ther. *17*, 607–613. https://doi.org/10.1038/mt.2009.3.

17. Uchida, A., Sasaguri, H., Kimura, N., Tajiri, M., Ohkubo, T., Ono, F., Sakaue, F., Kanai, K., Hirai, T., Sano, T., et al. (2012). Non-human primate model of amyotrophic lateral sclerosis with cytoplasmic mislocalization of TDP-43. Brain *135*, 833–846. https://doi.org/10.1093/brain/awr348.

18. Wils, H., Kleinberger, G., Janssens, J., Pereson, S., Joris, G., Cuijt, I., Smits, V., Ceuterick-de Groote, C., Van Broeckhoven, C., and Kumar-Singh, S. (2010). TDP-43 transgenic mice develop spastic paralysis and neuronal inclusions characteristic of ALS and frontotemporal lobar degen-

eration. Proc. Natl. Acad. Sci. USA *107*, 3858–3863. https://doi.org/10.1073/pnas.0912417107.

19. Xu, Y.F., Gendron, T.F., Zhang, Y.J., Lin, W.L., D'Alton, S., Sheng, H., Casey, M.C., Tong, J., Knight, J., Yu, X., et al. (2010). Wild-type human TDP-43 expression causes TDP-43 phosphorylation, mitochondrial aggregation, motor deficits, and early mortality in transgenic mice. J. Neurosci. *30*, 10851–10859. https://doi.org/10.1523/JNEUROSCI.1630-10.2010.

20. Ayala, Y.M., De Conti, L., Avendaño-Vázquez, S.E., Dhir, A., Romano, M., D'Ambrogio, A., Tollervey, J., Ule, J., Baralle, M., Buratti, E., and Baralle, F.E. (2011). TDP-43 regulates its mRNA levels through a negative feedback loop. EMBO J. *30*, 277–288. https://doi.org/10.1038/emboj.2010.310.

21. Polymenidou, M., Lagier-Tourenne, C., Hutt, K.R., Huelga, S.C., Moran, J., Liang, T.Y., Ling, S.C., Sun, E., Wancewicz, E., Mazur, C., et al. (2011). Long pre-mRNA depletion and RNA missplicing contribute to neuronal vulnerability from loss of TDP-43. Nat. Neurosci. *14*, 459–468. https://doi.org/10.1038/nn.2779.

22. Arnold, E.S., Ling, S.C., Huelga, S.C., Lagier-Tourenne, C., Polymenidou, M., Ditsworth, D., Kordasiewicz, H.B., McAlonis-Downes, M., Platoshyn, O., Parone, P.A., et al. (2013). ALS-linked TDP-43 mutations produce aberrant RNA splicing and adult-onset motor neuron disease without aggregation or loss of nuclear TDP-43. Proc. Natl. Acad. Sci. USA *110*, E736–E745. https://doi.org/10.1073/pnas.1222809110.

23. Sugai, A., Kato, T., Koyama, A., Koike, Y., Konno, T., Ishihara, T., and Onodera, O. (2019). Non-genetically modified models exhibit TARDBP mRNA increase due to perturbed TDP-43 autoregulation. Neurobiol. Dis. *130*, 104534. https://doi.org/10.1016/j.nbd.2019.104534.

24. D'Alton, S., Altshuler, M., and Lewis, J. (2015). Studies of alternative isoforms provide insight into TDP-43 autoregulation and pathogenesis. RNA *21*, 1419–1432. https://doi.org/10.1261/rna.047647.114.

25. Koyama, A., Sugai, A., Kato, T., Ishihara, T., Shiga, A., Toyoshima, Y., Koyama, M., Konno, T., Hirokawa, S., Yokoseki, A., et al. (2016). Increased cytoplasmic TARDBP mRNA in affected spinal motor neurons in ALS caused by abnormal autoregulation of TDP-43. Nucleic Acids Res. *44*, 5820–5836. https://doi.org/10.1093/nar/gkw499.

26. Chang, M., Lv, H., Zhang, W., Ma, C., He, X., Zhao, S., Zhang, Z.W., Zeng, Y.X., Song, S., Niu, Y., and Tong, W.M. (2017). Region-specific RNA m(6)A methylation represents a new layer of control in the gene regulatory network in the mouse brain. Open Biol. *7*, 170166. https://doi.org/10.1098/rsob.170166.

27. Meyer, K.D., Saletore, Y., Zumbo, P., Elemento, O., Mason, C.E., and Jaffrey, S.R. (2012). Comprehensive analysis of mRNA methylation reveals enrichment in 3' UTRs and near stop codons. Cell *149*, 1635–1646. https://doi.org/10.1016/j.cell.2012.05.003.

28. Nainar, S., Marshall, P.R., Tyler, C.R., Spitale, R.C., and Bredy, T.W. (2016). Evolving insights into RNA modifications and their functional diversity in the brain. Nat. Neurosci. *19*, 1292–1298. https://doi.org/10.1038/nn.4378.

29. Dominissini, D., Moshitch-Moshkovitz, S., Schwartz, S., Salmon-Divon, M., Ungar, L., Osenberg, S., Cesarkas, K., Jacob-Hirsch, J., Amariglio, N., Kupiec, M., et al. (2012). Topology of the human and mouse m6A RNA methylomes revealed by m6A-seq. Nature *485*, 201–206. https://doi.org/10.1038/nature11112.

30. Zhang, Z., Theler, D., Kaminska, K.H., Hiller, M., de la Grange, P., Pudimat, R., Rafalska, I., Heinrich, B., Bujnicki, J.M., Allain, F.H.T., and Stamm, S. (2010). The YTH domain is a novel RNA binding domain. J. Biol. Chem. *285*, 14701–14710. https://doi.org/10.1074/jbc.M110.104711.

31. Liu, N., Dai, Q., Zheng, G., He, C., Parisien, M., and Pan, T. (2015). N(6)-methyladenosine-dependent RNA structural switches regulate RNA-protein interactions. Nature *518*, 560–564. https://doi.org/10.1038/nature14234.

32. Dermentzaki, G., and Lotti, F. (2020). New Insights on the Role of N (6)-Methyladenosine RNA Methylation in the Physiology and Pathology of the Nervous System. Front. Mol. Biosci. *7*, 555372. https://doi.org/10.3389/fmolb.2020.555372.

33. Widagdo, J., and Anggono, V. (2018). The m6A-epitranscriptomic signature in neurobiology: from neurodevelopment to brain plasticity. J. Neurochem. *147*, 137–152. https://doi.org/10.1111/jnc.14481.

34. Mitropoulos, K., Merkouri Papadima, E., Xiromerisiou, G., Balasopoulou, A., Charalampidou, K., Galani, V., Zafeiri, K.V., Dardiotis, E., Ralli, S., Deretzi, G., et al. (2017). Genomic variants in the FTO gene are associated with sporadic amyotrophic lateral sclerosis in Greek patients. Hum. Genom. *11*, 30. https://doi.org/10.1186/s40246-017-0126-2.

35. Kim, H.J., Kim, N.C., Wang, Y.D., Scarborough, E.A., Moore, J., Diaz, Z., MacLea, K.S., Freibaum, B., Li, S., Molliex, A., et al. (2013). Mutations in prion-like domains in hnRNPA2B1 and hnRNPA1 cause multisystem proteinopathy and ALS. Nature *495*, 467–473. https://doi.org/10.1038/nature11922.

36. Yoneda, R., Ueda, N., and Kurokawa, R. (2021). m6A Modified Short RNA Fragments Inhibit Cytoplasmic TLS/FUS Aggregation Induced by Hyperosmotic Stress. Int. J. Mol. Sci. *22*, 11014. https://doi.org/10.3390/ijms222011014.

37. Poh, H.X., Mirza, A.H., Pickering, B.F., and Jaffrey, S.R. (2022). Alternative splicing of METTL3 explains apparently METTL3-independent m6A modifications in mRNA. PLoS Biol. *20*, e3001683. https://doi.org/10.1371/journal.pbio.3001683.

38. Geula, S., Moshitch-Moshkovitz, S., Dominissini, D., Mansour, A.A., Kol, N., Salmon-Divon, M., Hershkovitz, V., Peer, E., Mor, N., Manor, Y.S., et al. (2015). Stem cells. m6A mRNA methylation facilitates resolution of naive pluripotency toward differentiation. Science *347*, 1002–1006. https://doi.org/10.1126/science.1261417.

39. Lee, H., Bao, S., Qian, Y., Geula, S., Leslie, J., Zhang, C., Hanna, J.H., and Ding, L. (2019). Stage-specific requirement for Mettl3-dependent m(6)A mRNA methylation during haematopoietic stem cell differentiation. Nat. Cell Biol. *21*, 700–709. https://doi.org/10.1038/s41556-019-0318-1.

40. Daigle, T.L., and Caron, M.G. (2012). Elimination of GRK2 from cholinergic neurons reduces behavioral sensitivity to muscarinic receptor activation. J. Neurosci. *32*, 11461–11466. https://doi.org/10.1523/JNEUROSCI.2234-12.2012.

41. Pellegatta, M., Canevazzi, P., Forese, M.G., Podini, P., Valenzano, S., Del Carro, U., Quattrini, A., and Taveggia, C. (2022). ADAM17 Regulates p75(NTR)-Mediated Fibrinolysis and Nerve Remyelination. J. Neurosci. *42*, 2433–2447. https://doi.org/10.1523/JNEUROSCI.1341-21.2022.

42. Kaplan, A., Spiller, K.J., Towne, C., Kanning, K.C., Choe, G.T., Geber, A., Akay, T., Aebischer, P., and Henderson, C.E. (2014). Neuronal matrix metalloproteinase-9 is a determinant of selective neurodegeneration. Neuron *81*, 333–348. https://doi.org/10.1016/j.neuron.2013.12.009.

43. Morisaki, Y., Niikura, M., Watanabe, M., Onishi, K., Tanabe, S., Moriwaki, Y., Okuda, T., Ohara, S., Murayama, S., Takao, M., et al. (2016). Selective Expression of Osteopontin in ALS-resistant Motor Neurons is a Critical Determinant of Late Phase Neurodegeneration Mediated by Matrix Metalloproteinase-9. Sci. Rep. *6*, 27354. https://doi.org/10.1038/srep27354.

44. Hegedus, J., Putman, C.T., and Gordon, T. (2007). Time course of preferential motor unit loss in the SOD1 G93A mouse model of amyotrophic lateral sclerosis. Neurobiol. Dis. *28*, 154–164. https://doi.org/10.1016/j.nbd.2007.07.003.

45. Nagai, M., Re, D.B., Nagata, T., Chalazonitis, A., Jessell, T.M., Wichterle, H., and Przedborski, S. (2007). Astrocytes expressing ALS-linked mutated SOD1 release factors selectively toxic to motor neurons. Nat. Neurosci. *10*, 615–622. https://doi.org/10.1038/nn1876.

46. Wichterle, H., and Peljto, M. (2008). Differentiation of mouse embryonic stem cells to spinal motor neurons. Curr. Protoc. Stem Cell Biol. *Chapter 1*. https://doi.org/10.1002/9780470151808.sc01h01s5.

47. Wichterle, H., Lieberam, I., Porter, J.A., and Jessell, T.M. (2002). Directed differentiation of embryonic stem cells into motor neurons. Cell *110*, 385–397.

48. Simon, C.M., Janas, A.M., Lotti, F., Tapia, J.C., Pellizzoni, L., and Mentis, G.Z. (2016). A Stem Cell Model of the Motor Circuit Uncouples Motor Neuron Death from Hyperexcitability Induced by SMN Deficiency. Cell Rep. *16*, 1416–1430. https://doi.org/10.1016/j.celrep.2016.06.087.

49. Sorci, M., Ianniello, Z., Cruciani, S., Larivera, S., Ginistrelli, L.C., Capuano, E., Marchioni, M., Fazi, F., and Fatica, A. (2018). METTL3 regulates WTAP protein homeostasis. Cell Death Dis. *9*, 796. https://doi.org/10.1038/s41419-018-0843-z.

50. Ikiz, B., Alvarez, M.J., Ré, D.B., Le Verche, V., Politi, K., Lotti, F., Phani, S., Pradhan, R., Yu, C., Croft, G.F., et al. (2015). The Regulatory Machinery of Neurodegeneration in In Vitro Models of Amyotrophic Lateral Sclerosis. Cell Rep. *12*, 335–345. https://doi.org/10.1016/j.celrep.2015.06.019.

51. Mishra, V., Re, D.B., Le Verche, V., Alvarez, M.J., Vasciaveo, A., Jacquier, A., Doulias, P.T., Greco, T.M., Nizzardo, M., Papadimitriou, D., et al. (2020). Systematic elucidation of neuron-astrocyte interaction in models of amyotrophic lateral sclerosis using multi-modal integrated bioinformatics workflow. Nat. Commun. *11*, 5579. https://doi.org/10.1038/s41467-020-19177-y.

52. Zaccara, S., and Jaffrey, S.R. (2020). A Unified Model for the Function of YTHDF Proteins in Regulating m(6)A-Modified mRNA. Cell *181*, 1582–1595.e18. https://doi.org/10.1016/j.cell.2020.05.012.

53. McMillan, M., Gomez, N., Hsieh, C., Bekier, M., Li, X., Miguez, R., Tank, E.M.H., and Barmada, S.J. (2023). RNA methylation influences TDP43 binding and disease pathogenesis in models of amyotrophic lateral sclerosis and frontotemporal dementia. Mol. Cell *83*, 219–236.e7. https://doi.org/10.1016/j.molcel.2022.12.019.

54. Workman, R.E., Tang, A.D., Tang, P.S., Jain, M., Tyson, J.R., Razaghi, R., Zuzarte, P.C., Gilpatrick, T., Payne, A., Quick, J., et al. (2019). Nanopore native RNA sequencing of a human poly(A) transcriptome. Nat. Methods *16*, 1297–1305. https://doi.org/10.1038/s41592-019-0617-2.

55. Furlan, M., Delgado-Tejedor, A., Mulroney, L., Pelizzola, M., Novoa, E.M., and Leonardi, T. (2021). Computational methods for RNA modification detection from nanopore direct RNA sequencing data. RNA Biol. *18*, 31–40. https://doi.org/10.1080/15476286.2021.1978215.

56. Leger, A., Amaral, P.P., Pandolfini, L., Capitanchik, C., Capraro, F., Miano, V., Migliori, V., Toolan-Kerr, P., Sideri, T., Enright, A.J., et al. (2021). RNA modifications detection by comparative Nanopore direct RNA sequencing. Nat. Commun. *12*, 7198. https://doi.org/10.1038/s41467-021-27393-3.

57. Xia, Z., Tang, M., Ma, J., Zhang, H., Gimple, R.C., Prager, B.C., Tang, H., Sun, C., Liu, F., Lin, P., et al. (2021). Epitranscriptomic editing of the RNA N6-methyladenosine modification by dCasRx conjugated methyltransferase and demethylase. Nucleic Acids Res. *49*, 7361–7374. https://doi.org/10.1093/nar/gkab517.

58. Zeng, Y., Wang, S., Gao, S., Soares, F., Ahmed, M., Guo, H., Wang, M., Hua, J.T., Guan, J., Moran, M.F., et al. (2018). Refined RIP-seq protocol for epitranscriptome analysis with low input materials. PLoS Biol. *16*, e2006092. https://doi.org/10.1371/journal.pbio.2006092.

59. Koehler, L.C., Grese, Z.R., Bastos, A.C.S., Mamede, L.D., Heyduk, T., and Ayala, Y.M. (2022). TDP-43 Oligomerization and Phase Separation Properties Are Necessary for Autoregulation. Front. Neurosci. *16*, 818655. https://doi.org/10.3389/fnins.2022.818655.

60. Nijssen, J., Comley, L.H., and Hedlund, E. (2017). Motor neuron vulnerability and resistance in amyotrophic lateral sclerosis. Acta Neuropathol. *133*, 863–885. https://doi.org/10.1007/s00401-017-1708-8.

61. Ragagnin, A.M.G., Shadfar, S., Vidal, M., Jamali, M.S., and Atkin, J.D. (2019). Motor Neuron Susceptibility in ALS/FTD. Front. Neurosci. *13*, 532. https://doi.org/10.3389/fnins.2019.00532.

62. Wang, C.X., Cui, G.S., Liu, X., Xu, K., Wang, M., Zhang, X.X., Jiang, L.Y., Li, A., Yang, Y., Lai, W.Y., et al. (2018). METTL3-mediated m6A modification is required for cerebellar development. PLoS Biol. *16*, e2004880. https://doi.org/10.1371/journal.pbio.2004880.

63. Wang, Y., Li, Y., Yue, M., Wang, J., Kumar, S., Wechsler-Reya, R.J., Zhang, Z., Ogawa, Y., Kellis, M., Duester, G., and Zhao, J.C. (2018). N(6)-methyladenosine RNA modification regulates embryonic neural

stem cell self-renewal through histone modifications. Nat. Neurosci. *21*, 195–206. https://doi.org/10.1038/s41593-017-0057-1.

64. Xu, H., Dzhashiashvili, Y., Shah, A., Kunjamma, R.B., Weng, Y.L., Elbaz, B., Fei, Q., Jones, J.S., Li, Y.I., Zhuang, X., et al. (2020). m(6)A mRNA Methylation Is Essential for Oligodendrocyte Maturation and CNS Myelination. Neuron *105*, 293–309.e5. https://doi.org/10.1016/j.neuron.2019.12.013.

65. Shafik, A.M., Zhang, F., Guo, Z., Dai, Q., Pajdzik, K., Li, Y., Kang, Y., Yao, B., Wu, H., He, C., et al. (2021). N6-methyladenosine dynamics in neurodevelopment and aging, and its potential role in Alzheimer's disease. Genome Biol. *22*, 17. https://doi.org/10.1186/s13059-020-02249-z.

66. Bonanomi, D. (2019). Axon pathfinding for locomotion. Semin. Cell Dev. Biol. *85*, 26–35. https://doi.org/10.1016/j.semcdb.2017.11.014.

67. Bonanomi, D., and Pfaff, S.L. (2010). Motor axon pathfinding. Cold Spring Harbor Perspect. Biol. *2*, a001735. https://doi.org/10.1101/cshperspect.a001735.

68. Philippidou, P., and Dasen, J.S. (2013). Hox genes: choreographers in neural development, architects of circuit organization. Neuron *80*, 12–34. https://doi.org/10.1016/j.neuron.2013.09.020.

69. Li, Y., Dou, X., Liu, J., Xiao, Y., Zhang, Z., Hayes, L., Wu, R., Fu, X., Ye, Y., Yang, B., et al. (2023). Globally reduced N(6)-methyladenosine (m(6)A) in C9ORF72-ALS/FTD dysregulates RNA metabolism and contributes to neurodegeneration. Nat. Neurosci. *26*, 1328–1338. https://doi.org/10.1038/s41593-023-01374-9.

70. Durinck, S., Moreau, Y., Kasprzyk, A., Davis, S., De Moor, B., Brazma, A., and Huber, W. (2005). BioMart and Bioconductor: a powerful link between biological databases and microarray data analysis. Bioinformatics *21*, 3439–3440. https://doi.org/10.1093/bioinformatics/bti525.

71. Durinck, S., Spellman, P.T., Birney, E., and Huber, W. (2009). Mapping identifiers for the integration of genomic datasets with the R/Bioconductor package biomaRt. Nat. Protoc. *4*, 1184–1191. https://doi.org/10.1038/nprot.2009.97.

72. Love, M.I., Huber, W., and Anders, S. (2014). Moderated estimation of fold change and dispersion for RNA-seq data with DESeq2. Genome Biol. *15*, 550. https://doi.org/10.1186/s13059-014-0550-8.

73. Cui, X., Wei, Z., Zhang, L., Liu, H., Sun, L., Zhang, S.W., Huang, Y., and Meng, J. (2016). Guitar: An R/Bioconductor Package for Gene Annotation Guided Transcriptomic Analysis of RNA-Related Genomic Features. BioMed Res. Int. *2016*, 8367534. https://doi.org/10.1155/2016/8367534.

74. Bailey, T.L., Johnson, J., Grant, C.E., and Noble, W.S. (2015). The MEME Suite. Nucleic Acids Res. *43*, W39–W49. https://doi.org/10.1093/nar/gkv416.

75. Wu, T., Hu, E., Xu, S., Chen, M., Guo, P., Dai, Z., Feng, T., Zhou, L., Tang, W., Zhan, L., et al. (2021). clusterProfiler 4.0: A universal enrichment tool for interpreting omics data. Innovation *2*, 100141. https://doi.org/10.1016/j.xinn.2021.100141.

76. Yu, G., Wang, L.G., Han, Y., and He, Q.Y. (2012). clusterProfiler: an R package for comparing biological themes among gene clusters. OMICS *16*, 284–287. https://doi.org/10.1089/omi.2011.0118.

77. Kishore, K., de Pretis, S., Lister, R., Morelli, M.J., Bianchi, V., Amati, B., Ecker, J.R., and Pelizzola, M. (2015). methylPipe and compEpiTools: a suite of R packages for the integrative analysis of epigenomics data. BMC Bioinf. *16*, 313. https://doi.org/10.1186/s12859-015-0742-6.

78. Loman, N.J., Quick, J., and Simpson, J.T. (2015). A complete bacterial genome assembled de novo using only nanopore sequencing data. Nat. Methods *12*, 733–735. https://doi.org/10.1038/nmeth.3444.

79. Mulas, C., Kalkan, T., von Meyenn, F., Leitch, H.G., Nichols, J., and Smith, A. (2019). Defined conditions for propagation and manipulation of mouse embryonic stem cells. Development *146*, dev173146. https://doi.org/10.1242/dev.173146.

80. Lotti, F., Menguzzato, E., Rossi, C., Naldini, L., Ailles, L., Mavilio, F., and Ferrari, G. (2002). Transcriptional targeting of lentiviral vectors by long terminal repeat enhancer replacement. J. Virol. *76*, 3996–4007.

81. Li, H. (2018). Minimap2: pairwise alignment for nucleotide sequences. Bioinformatics *34*, 3094–3100. https://doi.org/10.1093/bioinformatics/bty191.

82. Li, H., Handsaker, B., Wysoker, A., Fennell, T., Ruan, J., Homer, N., Marth, G., Abecasis, G., and Durbin, R.; 1000 Genome Project Data Processing Subgroup (2009). The Sequence Alignment/Map format and SAMtools. Bioinformatics *25*, 2078–2079. https://doi.org/10.1093/bioinformatics/btp352.

83. Hallegger, M., Chakrabarti, A.M., Lee, F.C.Y., Lee, B.L., Amalietti, A.G., Odeh, H.M., Copley, K.E., Rubien, J.D., Portz, B., Kuret, K., et al. (2021). TDP-43 condensation properties specify its RNA-binding and regulatory repertoire. Cell *184*, 4680–4696.e22. https://doi.org/10.1016/j.cell.2021.07.018.

84. Gene Ontology Consortium (2021). The Gene Ontology resource: enriching a GOld mine. Nucleic Acids Res. *49*, D325–D334. https://doi.org/10.1093/nar/gkaa1113.

85. Kanehisa, M. (2019). Toward understanding the origin and evolution of cellular organisms. Protein Sci. *28*, 1947–1951. https://doi.org/10.1002/pro.3715.

86. Kanehisa, M., Furumichi, M., Sato, Y., Ishiguro-Watanabe, M., and Tanabe, M. (2021). integrating viruses and cellular organisms. Nucleic Acids Res. *49*, D545–D551. https://doi.org/10.1093/nar/gkaa970.

87. Kanehisa, M., and Goto, S. (2000). KEGG: kyoto encyclopedia of genes and genomes. Nucleic Acids Res. *28*, 27–30. https://doi.org/10.1093/nar/28.1.27.

STAR★METHODS

KEY RESOURCES TABLE

REAGENT or RESOURCE	SOURCE	IDENTIFIER
Antibodies		
Rabbit polyclonal anti-m6A	Synaptic Systems	Cat#202003; RRID: AB_2279214
Rabbit monoclonal anti-METTL3	Abcam	Cat#AB_195352; RRID: AB_2721254
Mouse monoclonal anti-β-ACTIN	Sigma-Aldrich	Cat#A5441; RRID:AB_476744
Mouse monoclonal anti-TUJ1	BioLegend	Cat#801213; RRID:AB_2728521
Goat polyclonal anti-ChAT	Millipore	Cat#AB114P; RRID:AB_2313845
Goat polyclonal anti-MMP9	Sigma-Aldrich	Cat#M9570; RRID:AB_1079397
Rabbit polyclonal anti-GFAP	Agilent	Cat#Z0334; RRID:AB_10013382
Guinea pig polyclonal anti-Synaptophysin	Project ALS/Antibody Core (custom-made)	N/A
Alexa Fluor 488 Alpha-Bungarotoxin conjugate	Invitrogen	Cat#B13422
Rabbit Polyclonal anti-TDP-43	Proteintech	Cat#10782-2-AP; RRID:AB_615042
Rabbit polyclonal anti-Histone-H3	Proteintech	Cat#17168-1-AP; RRID:AB_2716755
Rabbit monoclonal anti-GAPDH	Cell Signaling Techonology	Cat #2118 RRID:AB_561053
Bacterial and virus strains		
One Shot™ Stbl3™ Chemically Competent *E. coli*	Invitrogen	Cat#C737303
Chemicals, peptides, and recombinant proteins		
Leukemia inhibitory factor (LIF)	Chemicon ESGRO	Cat#ESG1107
GDNF	Reprotech	Cat#450-10
CNTF	Reprotech	Cat#450-13
BDNF	Reprotech	Cat#450-02
Critical commercial assays		
Power Green Master Mix	Applied biosystems	Cat#4367659
RevertAid First Strand cDNA Synthesis Kit	Thermo Scientific	Cat#K1691
RNeasy mini kit	Qiagen	Cat#74106
Dynabeads mRNA purification kit	Invitrogen	Cat#61006
Direct RNA Sequencing kit	Nanopore store	Cat#RNA002
Deposited data		
Direct RNA Sequencing Runs	NCBI	SRA: PRJNA901684
Codes	GitHub	GitHub: https://github.com/mfurla/Dermentzaki_CellReports_2024/releases/tag/R2
Codes	Zenodo	Zenodo: https://doi.org/10.5281/zenodo.10657218
Raw data	Mendeley Data	Mendeley Data: https://doi.org/10.17632/g3hjnsygs7.1
Experimental models: Cell lines		
Hb9:eGFP mouse ES cell line	(Wichterle et al.)[47]	N/A
Stable HEK293^{TDP-43}	(Koehler et al.)[59]	N/A
Experimental models: Organisms/strains		
Mettl3 floxed mice	(Geula et al.)[38] (Lee et al.)[39]	C57BL/6
B6.129S-*Chat$^{tm1(cre)Lowl}$*/MwarJ	The Jackson Laboratory	Strain#031661; RRID: IMSR_JAX:031661
Oligonucleotides		
All RT-(q)PCR primers are reported in Table S2	This study	N/A
For all siRNA/shRNA sequences check Table S2	This study	N/A
Tardbp Prime Time qPCR primers Mm. PT 58.5553804, exon location 2-3	IDT	Cat#447472065

Continued

REAGENT or RESOURCE	SOURCE	IDENTIFIER
For all guide RNA and HDR oligo sequences for CRISPR/Cas9 deletion of Mettl3 check Table S2	This study	N/A
siRNA 1-ON-TARGET plus siRNA METTL3 (Human) SMARTPool	Horizon 22 Discovery, Dharmacon	N/A
Nontargeting siRNA #1	Horizon 22 Discovery, Dharmacon	N/A
Recombinant DNA		
lentiCRISPR v2 plasmid	Addgene	RRID:Addgene_52961
pLKO.1-puro vector	Sigma MISSION	Cat#SHC001
pLKO.1-puro Non-Mammalian shRNA control transduction particles	Sigma MISSION	Cat#SHC002H
pLKO.1-Ythdf1	Sigma MISSION	TRCN0000348429
pLKO.1-Ythdf2	Sigma MISSION	TRCN0000197932
pLKO.1-Ythdf3	Sigma MISSION	TRCN0000329409
pLKO.1-Mettl3	Sigma MISSION	TRCN0000039111
pcDNA3-flag-YTHDF2	Addgene	RRID:Addgene_52300
pcDNA-FLAG-METTL3	Addgene	RRID:Addgene_53739
pcDNA-FLAG-METTL3-APPA	Addgene	RRID:Addgene_160251
pRRL-CMV-flag-YTHDF2	This study	N/A
pRRL-CMV-FLAG-METTL3	This study	N/A
pRRL-CMV-FLAG-METTL3-APPA	This study	N/A
Software and algorithms		
GraphPad Prism 9.2.0	GraphPad	https://www.graphpad.com/features
Fiji (ImageJ)	NIH	https://imagej.nih.gov/ij/
Adobe Photoshop	Adobe	https://adobe.com
Nanocompore	(Leger et al.)[56]	https://github.com/tleonardi/nanocompore_pipeline
biomaRt, v2.42.0	(Durinck et al.)[70] (Durinck et al.)[71]	https://dec2021.archive.ensembl.org:443/biomart/martservice
DESeq2, v1.26.0	(Love et al.)[72]	https://doi.org/10.18129/B9.bioc.DESeq2
MinKNOW (v19.12.6)	Oxford Nanopore	N/A
Guitar package (v2.2.0)	(Cui et al.)[73]	https://doi.org/10.18129/B9.bioc.Guitar
MEME suite	(Bailey et al.)[74]	https://meme-suite.org/meme/
clusterProfiler, v3.14.3	(Wu et al.)[75] (Yu et al.)[76]	https://doi.org/10.18129/B9.bioc.clusterProfiler
compEpiTools, v1.20.0	(Kishore et al.)[77]	https://doi.org/10.18129/B9.bioc.compEpiTools
Nanopolish, v0.13.2	(Loman et al.)[78]	https://github.com/jts/nanopolish
NanopolishComp, v0.6.11	(Leger et al.)[56]	https://github.com/a-slide/NanopolishComp
Guppy v3.2.10	Oxford Nanopore	N/A
pycoQC (2.5.0.21)	(Leger et al.)[56]	https://github.com/a-slide/pycoQC
Minimap2 (v2.10-r761)	(Li et al.)[79]	https://github.com/lh3/minimap2
GRCm38.p6	Ensembl Genome browser	http://nov2020.archive.ensembl.org/Mus_musculus/Info/Index

RESOURCE AVAILABILITY

Lead contact

Further information and requests for resources and reagents should be directed to and will be fulfilled by the lead contact, Francesco Lotti (fl2219@cumc.columbia.edu).

Materials availability

All unique reagents generated in this study are available from the Lead Contact with a completed Materials Transfer Agreement.

Data and code availability

- Nanopore sequencing data have been deposited at GEO with project ID PRJNA901684 and will be publicly available as of the date of publication. Raw data as original western blot images are deposited at Mendeley Data (https://doi.org/10.17632/g3hjnsygs7.1). The lead contact will share all other types of data reported in this paper upon request.
- The supplemental file Data S1 contains the code used to generate the results and Figures 4 and S4. The same code is also available on GitHub (https://github.com/mfurla/Dermentzaki_CellReports_2024/releases/tag/R2) and Zenodo (https://doi.org/10.5281/zenodo.10657218).
- Any additional information required to reanalyze the data reported in this paper is available from the lead contact upon request.

EXPERIMENTAL MODEL AND STUDY PARTICIPANT DETAILS

Animals

All experimental procedures and designs followed the National Institutes of Health Guide for Care and Use of Laboratory Animals (National Research Council, 2011) and ARRIVE guidelines. All animal procedures were approved and performed following the institutional animal care and use committee's policies at Columbia University. Male and female mice were group-housed in polycarbonate cages with corncob bedding; they were maintained in a humidity-and temperature-controlled vivarium (20-22°C) on a 12/12 h light/dark schedule. Animals had access *ad libitum* to food and water except during behavioral testing. All experiments requiring wild-type mice will use C57BL/6J mice from Jackson Laboratories (Stock No: 000664). Mettl3 floxed mice *(Mettl3$^{fl/fl}$)*[38,39] were kindly provided by Dr. Lei Ding at Columbia University. *Mettl3$^{fl/fl}$* bred with B6.129S-*Chat$^{tm1(cre)Lowl}$*/MwarJ (JAX # 031661) mice to generate *Mettl3$^{fl/fl}$;*ChAT::Cre mice. *Mettl3* and ChATCre genotyping was performed with specific primers: Mettl3 floxed F'; Mettl3 floxed R'; ChATCre WT; ChATCre Common; ChATCre Mutant (see Table S2).

Mouse embryonic stem cells (mESCs) cultures

We used Embryonic Stem Cells (ESCs) of mouse origin in this study. Mouse ESCs expressing a motor neuron-specific reporter (Hb9:eGFP) were established as previously described.[47] The authenticity of these cells is confirmed by monitoring the efficiency of directed differentiation into motor neurons using the appropriate assays (usually immunohistochemistry and flow cytometry). ES cells were grown under standard pluripotency maintenance conditions on DR4 irradiated mouse embryonic fibroblast feeder cells (GlobalStem) seeded on 0.1% gelatinized (Millipore, #ES 006-B) tissue culture plates. ES cells were cultured in N2B27 2i/LIF conditions[38,79]: 50% Neurobasal medium (Gibco, #21103), 50% DMEM/F12 (Gibco, #12634), 2 mM L-Glutamine (Gibco, #25030-081), 0.1 mM β-mercaptoethanol (Milipore, #ES-007-E), NDiff Neuro-2 Medium Supplement (Millipore, SCM012), B-27 Medium Supplement (Gibco, #12587-010), 1,000 U ml^{-1} LIF, 3 μM GSK3 inhibitor (CHIR99021, Tocris Cat. # 4423), 1 μM MEK inhibitor (PD0325901, Tocris Cat. # 4192).

METHOD DETAILS

mESCs differentiation into MNs and lentiviral transduction

For motor neuron differentiation, at DIV 3, ES cells were trypsinized with 1X trypsin/EDTA (Gibco, #25300120) and cultured in αDFNK media: 1:1 DMEM/F12 (Gibco, #12634) and Neurobasal A (Gibco, #21103); 10% Knock-out serum (Invitrogen, #10828-028); Glutamine (Gibco, #25030-081); β-Mercaptoethanol (Millipore, #ES-007-E); Pen/Strep (Gibco, #15140-112). At DIV 4, forming embryonic bodies (EBs) were transferred in low-adherence plates (TC falcon). At DIV 5, 1 μM of all-*trans* retinoic acid (RA, Sigma, #R2625) and 0.25 μM of smoothened agonist (SAG, Calbiochem, #566660) were added for an additional 4 days. Next, differentiated EBs were dissociated and/or FACS-sorted and plated in 96-well plates at a density of 4,000 cells/well in ES-MN media: Neurobasal media (Gibco, (#ME120079L2); B27 (Gibco, #12587-010); Horse serum (Gibco, #26050-070); Glutamine (Gibco, #25030-081); β-Mercaptoethanol (Milipore, #ES-007-E); Pen/Strep (Gibco, #15140-112); GDNF, CNTF, BDNF (10 ng/mL, Reprotech). ES-MN cultures (Cont and Mettl3-KO) were imaged every other day using an automated reader system (TROPHOS). MN number and neurite length was assessed with the MetaMorph software.

All shRNAs used in this study were cloned into the pLKO.1-puro vector (Sigma MISSION; Table S2). As non-targeting control (NTC) the pLKO.1-puro Non-Mammalian shRNA control transduction particles were used (SHC002H). ES-MNs cultures (4,000 cells/96-well plates) were transduced with an MOI:10 at DIV3, and live images were acquired from DIV4-DIV8 to assess MN number and neurite outgrowth. For METTL3, METTL3-APPA, and YTHDF2 expression, we obtained the plasmids from Addgene (see key resource table) and subcloned them in a pRRL-CMV lentiviral vector.[80]

METTL3 downregulation and TDP-43 autoregulation

The stable HEK293^{TDP-43} cell line expressing human TDP-43 upon tetracycline induction was generated as described.[59] Cells were maintained in DMEM (Dulbecco's Modified Eagle's Medium – high glucose) with 10% FBS (fetal bovine serum), 75ug/mL hygromycin

and incubated at 37°C and 5% CO_2. Downregulation of *METTL3* expression was achieved using specific siRNA 1-ON-TARGET plus siRNA *METTL3* (Human) SMARTPool and Nontargeting siRNA #1 was used as control (Horizon Discovery, Dharmacon). *METTL3* downregulation was measured by RT-qPCR using primers reported in Table S2. Cells were transfected twice, 24 h apart, using Oligofectamine Transfection Reagent (Thermo Fisher) according to manufacturer instructions. Cells were then induced with tetracycline (1 μg/μL) for 48 h. TDP-43 autoregulation was measured by quantification of endogenous TDP-43 protein and mRNA via immunoblotting and RT-qPCR, respectively, as described.[59]

CRISPR-Cas9 mediated Mettl3 knock-out in Hb9:eGFP ES cells
For Mettl3 knock-out, we used the lentiCRISPR v2 system (Addgene #52961) and 2 guide RNA sequences targeting *Mettl3* exon 4: *Mettl3* gRNA seq 1 (5′ of exon4) and *Mettl3* gRNA seq 2 (3′ of exon 4) (Table S2).

For cloning the guide RNAs into the lentiCRISPR v2 plasmid we used the GeCKO Lentiviral CRISPR toolbox Protocol. Briefly, we digested (BsmBI) and dephosphorylated 5 μg of the lentiCRISPR v2 plasmid. Next, we gel purified the digested the lenti-plasmid using the QIAquick Gel Extraction kit (Qiagen, #28706). In parallel, we phosphorylated and annealed each pair of Mettl3 guide oligos: Pair 1 primers (*Mettl3* gRNA seq1 F′, *Mettl3* gRNA seq1 R′); Pair 2 primers (*Mettl3* gRNA seq2 F′, *Mettl3* gRNA seq2 R′) (Table S2). Then, we ligated the annealed guide oligos with the lentiCRISPR v2 plasmid using the 2X Quick ligase (NEB, #M2200S) and transformed the ligated plasmids into Stbl3 bacteria. Bacterial colonies were PCR screened and sequenced for the right clones. Next, we transfected Hb9:eGFP ES cells (plated in a 6-well plate at different densities) with both *Mettl3* guide RNA; lentiCRISPR v2 plasmids together with a homology directed repair (HDR) oligo targeting upstream and downstream of the gRNA sequences (Table S2) using lipofectamine 3000 (Invitrogen, #L3000). Next day, we added fresh media supplemented with the selection marker puromycin (1 μg/mL). After 4 days, we trypsinized the surviving cells and transferred them at a low density (10,000/20,000 cells) in 10 cm plates containing ES media plus puromycin. When colonies started to grow, we transferred individual clones in 96-well plates and let them grow for a few days. Genomic DNA extraction was performed with the PureLink Genomic DNA kit (K1820-02, Invitrogen). Briefly, we thawed the 96-well plates and added 50 μL/well digestion buffer plus 1 mg/ml Proteinase K. We incubated the plates at 60C for 4 h, cooled down the plates on ice, added 50 μL/well lysis buffer and mixed by pipetting. Next, we added 150 μL of ice-cold ethanol, mixed by pipetting, and spanned the plates at 4C for 30 min at 2,500 x g. We decanted the liquid (by inverting the plate) and repeated the ethanol wash step at RT for 15 min at 2,500 x g. Again, we decanted the liquid and let the plate air dry at RT. Finally, we resuspended the DNA pellet in 200 μL of sterile ddH_2O and incubated the plates at 37C for at least 1 h. For colony PCR screening of Mettl3-KO clones, we diluted the DNA (1/10) and used the Green GoTaq master mix together with specific primers (*Mettl3*-KO F′, *Mettl3*-KO R′) (see Primer Table).

RNA extraction-cDNA synthesis-qPCR
Total RNA was extracted from mES-MNs using TRIzol reagent (Invitrogen, #15596). DNase treatment (M6101; Promega) was followed by phenol-chloroform extraction to ensure high RNA quality. RNA concentration was determined spectrophotometrically at 260nm. The quality of the RNA was determined by the 260/280 and 260/230 ratios. cDNA was generated with the RevertAid First Strand cDNA Synthesis Kit (K1691; ThermoFisher) following the manufacturer's instructions. For each reaction, we used 1 μg of RNA primed with both random hexamers and oligo(dT) primers. A three-step real-time qPCR was carried out with the QuantStudio 3 (Thermo Fisher) qPCR machine using the Power Green Master Mix (Applied Biosystems, #4367659).

m⁶A MeRIP
We performed an m⁶A MeRIP assay according to Zeng et al. 2018 with few modifications. Briefly, Dynabeads protein A (50 μL) (Invitrogen, #10001D), were washed twice in IP buffer [150 mM NaCl, 10 mM Tris-HCl pH 7.5, 0.1% IGEPAL CA-630 in nuclease free water], resuspended in 500 μL of IP buffer containing 5 μg of anti-m6A antibody (Synaptic Systems, #202 003) and incubated for 2h at 4C, under rotation. Following 2X washes in IP buffer, the beads-Ab mixture was resuspended in 500 μL of IP buffer containing 5 μg RNA (derived from Mettl3 WT or KO EBs) and 5 μL RNasin Plus RNase Inhibitor (Promega, #N2611) and incubated o/n at 4C. Next day, the reaction mixture was washed 2X with IP buffer, 2X with high salt IP buffer (500 mM NaCl,10 mM Tris-HCl pH 7.5, 0.1% IGEPAL CA-630 in nuclease-free water), and 1X wash in IP buffer for 10 min each at 4C under rotation. The m6A-enriched RNA was eluted from the beads in 200 μL of RLT buffer supplied in the RNeasy mini kit (Qiagen, #74106) for 2 min at RT. The supernatant was collected to a new tube, 400 μL of 100% ethanol was added, and the mixture was transferred to the RNeasy MiniElute spin column and centrifuged at 16.000 X G at 4C for 1 min. The spin column membrane was washed with 500 μL of RPE buffer once, then 500 μL of 80% ethanol, and centrifuged at full speed for 5 min at 4C. The m6A-enriched RNA was eluted with 20 μL RNase-free water. A total RNA sample was used for cDNA synthesis, and a qPCR assay was performed as described above.

Profiling the m⁶A epitranscriptome
ES-MNs (WT and KO) were FACS sorted, and total RNA was extracted using the TRIzol reagent (see above). According to the manufacturer's instructions, mRNA purification from total RNA was performed using the Dynabeads mRNA purification kit (Invitrogen, #61006). mRNA quality and lack of degradation were assessed with Bioanalyzer. dRNA-seq libraries were prepared according to the standard ONT protocol (kit RNA002) and sequenced on a GridION machine running MinKNOW v19.12.6; a flowcell was used for each sample (FLO-MIN106).

The current intensity signals were base called with Guppy (v3.2.10+aabd4ec - default options), and the quality of each run was checked with pycoQC (2.5.0.21). Pass reads (read quality score >7) were aligned to the mouse mm10 transcriptome with Minimap2 (v2.10-r761 - map-ont configuration),[81] and the resulting bam files were filtered with samtools[82] ("samtools view -F 2324" command) to remove unmapped reads, reads mapped to the reverse strand, not primary alignments and supplementary alignments. The reference transcriptome was obtained with bedtools getfasta (v2.26.0) using the GRCm38.p6 genome fasta and the corresponding annotation gtf file (http://nov2020.archive.ensembl.org/Mus_musculus/Info/Index). The reads were re-squiggled to the Nanopore ionic-current signal using Nanopolish (v0.13.2),[78] and the resulting output was post-processed with NanopolishComp (v0.6.11).[56] Nanocompore (v1.0.0rc3-1-dev)[56] was used to identify m6A+ 5-mers using default parameters (min_coverage 30, pvalue_thr 0.05, sequence_context 2, downsample_high_cov 5000) as described in detail at https://github.com/tleonardi/nanocompore_pipeline.

Two custom scripts available as supplemental material were used to process the Nanocompore output database and the Nanopolish eventalign tsv matrix in order to extract the modification probabilities of each TARDBP site at single read resolution (singleSiteProbabilities.py and singleMolecule.R).

Additional bioinformatic analyses

The supplemental file Data S1 contains the code used to generate the results and Figures 4 and S4. In particular, human TDP43 targets were defined as the 1,000 genes with the highest iCLIP sites density according to the dataset released in[83]; homologous genes in mouse were identified with biomaRt (v2.42.0 - getLDS function with mart host https://dec2021.archive.ensembl.org:443/biomart/martservice).[70,71] The same database was used for any ID conversion (i.e., Ensembl transcript ID to gene ID, Ensembl gene ID to symbol). Gene-level and transcript-level expressions were defined based on the alignment of the reads to the transcriptome. DESeq2 (v1.26.0)[72] was used for the normalization of transcriptional data and quantification of differential gene expression (adjusted p value <0.05). m6A+ 5-mers were identified according to the GMM logit-adjusted p value returned by Nanocompore with a threshold of 0.05. To define TARDBP m6A + sites, in the case of overlapping 5-mers, we selected the one with an A at the center (i.e., in position 3). The exact Fischer test implemented in the stats package (R 3.6.1) was used to detect overlaps between differentially expressed genes, TDP43 targets, and m6A + genes. The Wilcoxon test implemented in the stats package (R v3.6.1) was used to compare distributions. The Guitar package (v2.2.0)[73] was used to plot the distribution of methylated sites on the metagene. The online MEME suite[74] was used to detect motif enrichments for methylated and un-methylated 5-mers (complete output available in the supplemental file Data S1). Finally, clusterProfiler (v3.14.3)[75,76] and compEpiTools (v1.20.0)[77] were used to find enrichments for expressed genes and methylated genes in Gene Ontology[84] and KEGG pathways.[85–87]

Western blotting

WT and KO ES-MNs were lysed in RIPA buffer containing protease (Roche, #11836170001) and phosphatase inhibitors (Roche, #4906845001). Protein concentrations were determined with the Bradford assay (Bio-Rad). Proteins (30 μg)—mixed with 4X NuPAGE LDS sample buffer (Thermo Fisher, #NP0007) and 10X NuPAGE sample reducing agent (Thermo Fisher, #NP0004)—were separated on 4–12% Bis-Tris mini protein gels (Thermo Fisher, #NP0336) and then transferred to a 0.45 μm nitrocellulose membrane (Amersham, #10600002). NuPAGE antioxidant (Thermo Fisher, #NP0005) was added in both running (Thermo Fisher, #NP0001) and transfer buffer. Primary antibodies: METTL3 (Abcam, #195352); β-ACTIN (Sigma, #A5441). Secondary antibody: Rabbit and mouse HRP (GE Healthcare). Immunoblot signal was detected via chemiluminescence using the SuperSignal West Pico PLUS Chemiluminescent Substrate (Thermo Fisher, #34579).

Immunocytochemistry and immunohistochemistry

ES-INs (WT and KO) in 96-well plates were fixed in 4% PFA (Electron Microscopy Sciences 16% Paraformaldehyde Aqueous Solution, EM Grade, #15710) for 20 min at 4°C. Cells were washed 3X with PBS, blocked with 5% donkey serum (DS)/0.1% TBS-T (Jackson ImmunoResearch, #017-000-121) for 1h, and immunolabeled with the neuronal marker TUJ1 (1/1000, Biolegend, #801201) in 5% DS/0.1% TBS-T, overnight at 4°C. Next day, cells were washed 2X in 0.1% TBS-T, incubated with secondary antibody Alexa 594 (Invitrogen) in 5% DS/0.1% TBS-T for 1h at RT, washed 2X in 0.1% TBS-T, and 1X in PBS. Images were obtained using the TROPHOS high throughput imaging system.

Control and Mettl3-cKO mice were anesthetized (ketamine-xylazine) and perfused intracardially with 0.1 M ice-cold PBS (4 min, 10 mL/min) followed by ice-cold 4% PFA (Electron Microscopy Sciences 16% Paraformaldehyde Aqueous Solution, EM Grade, #15710-S) in 0.1 M PB (6 min, 10 mL/min). Brains and spinal cords were dissected, post-fixed in 4% PFA (4°C, overnight), washed 3X in PBS, and kept in PBS until vibratome processing. TA muscles were dissected, washed 3X in PBS, and kept in 30% sucrose until cryostat-cut processing.

For MN quantification

L4-L5 SC segments and/or midbrains were mounted on 4% agarose (Bioexpress, #E−3120-500) and cut on a vibratome (70 μm section thickness). Free-floating sections were blocked in 5% DS/0.4% TBS-T for 1h, and immunolabelled with primary antibodies against ChAT (1/200, Millipore, #AB-144P); Mmp9 (1/500, Sigma, M9570) and GFAP (1/1000, Dako, #20334) in 5% DS/0.4% TBS-T under rotation for 72 h at 4°C. Sections were washed 3X in 0.4% TBS-T, incubated with secondary antibodies: Alexa Fluor 488/594 (Invitrogen) in 5% DS/0.4% TBS-T under rotation for 3h at RT, and washed 3X in 0.4% TBS-T. Sections were slide-mounted (Fisher Scientific, # 12-550-15) with Fluoromount G (Invitrogen, # 00495802), and images were obtained at an Sp8 Leica confocal

microscope at 20X magnification. An entire set of a minimum of 15 sections from the L4-L5 segment and 8-10 sections from the midbrain were used to assess the average number of MNs (per hemisection).

For NMJ quantification

TA muscles were frozen in OCT (Tissue-Tek) with dry ice, and stored at −80°C. TA muscles were cryosectioned (20 μm) and slide-mounted (Fisher Scientific, # 12-550-15). NMJs were blocked in 5% DS/0.1% TBS-T for 1h and immunolabeled for the presynaptic marker Synaptophysin (Project ALS/Antibody Core, guinea pig) in 5% DS/0.1% TBS-T at 4°C, overnight. The next day, sections were washed 3X in 0.1% TBS-T, incubated with the postsynaptic marker α-bungarotoxin (BTX) (1/000, Invitrogen, #B13422) in 5% DS/0.1% TBS-T for 3h at RT, washed 3X in 0.1% TBS-T and mounted with Fluoromount G (Invitrogen, # 00495802). Images were obtained at an Sp8 Leica confocal microscope at 10X (for counting) and 40X (representative images) magnification. NMJ innervation was quantified by identifying BTX-positive NMJs (red) and determining the extent of colocalization with synaptophysin (green). Full innervation was considered when ≤70% overlap of BTX and synaptophysin was observed. At least 100 NMJs on 20 μm TA sections were imaged and counted for each genotype.

Mouse behavioral tests

Inverted grid or "wire-hang" test was performed by allowing the mouse to grip a grid—a square metal mesh—and then inverting the grid (180°), thus allowing the mouse to hang (Tillerson et al., 2002; Tillerson and Miller, 2003). The score was recorded as maximum hold time up to 120 s, as the best of three trials with at least 3 min resting period between each trial. Animals were tested once per week at roughly the same time of day throughout the trial.

Rotarod was performed using the rotarod apparatus (Ugo Basile). The rotarod is an automated apparatus with a 3–7 cm diameter "grooved rod," speed controls, and a lever that triggers the timer to stop once the mouse falls from the rod. This test requires mice to balance on a rotating rod, and their latency to fall is recorded as the endpoint measure. Mice are initially trained to stay on the rod at a constant rotation speed of 4 rpm for up to 2 min. Trained mice are tested every two weeks on a gradually accelerating rotarod; rotation speed begins at 5 rpm and is accelerated up to 40 rpm over 5 min. The latency to fall off the rotarod is recorded. Mice are tested for three trials before returning to their home cage (Brooks and Dunnett, 2009; Borse et al., 2011).

Open field was performed at the Mouse Neurobehavioral Core at Columbia according to published protocols (Yu et al., 2021; Cho et al., 2021). Each mouse was gently placed in the center of a clear Plexiglas arena (Med Associates, ENV-510) lit with dim light (∼5 lux), and was allowed to ambulate freely. Infrared (IR) beams embedded along the x, y, z axes of the arena automatically track distance moved, horizontal movement, vertical movement, stereotypies, and time spent in the center zone. Exploration was monitored during a 30 min session with Activity Monitor Version 7 tracking software (Med Associates Inc.). Data were analyzed in six, 5-min time bins. Areas were cleaned with 70% ethanol and thoroughly dried between trials.

QUANTIFICATION AND STATISTICAL ANALYSIS

Continuous variables were reported as percentages or means ± standard error of the mean (SEM), as appropriate. Differences among means were analyzed by one-way ANOVA. When the ANOVA showed significant differences, pairwise comparisons between means were assessed using Tukey's post hoc testing. All analyses rejected the null hypothesis at the 0.05 level and reported as follows: * = $p < 0.05$; ** = $p < 0.01$; *** = $p < 0.001$; **** = $p < 0.0001$. All analyses were performed with GraphPad Prism versions 7 and 9 (GraphPad Inc. La Jolla CA, USA).

Supplemental information

Depletion of *Mettl3* in cholinergic neurons

causes adult-onset neuromuscular degeneration

Georgia Dermentzaki, Mattia Furlan, Iris Tanaka, Tommaso Leonardi, Paola Rinchetti, Patricia M.S. Passos, Alliny Bastos, Yuna M. Ayala, Jacob H. Hanna, Serge Przedborski, Dario Bonanomi, Mattia Pelizzola, and Francesco Lotti
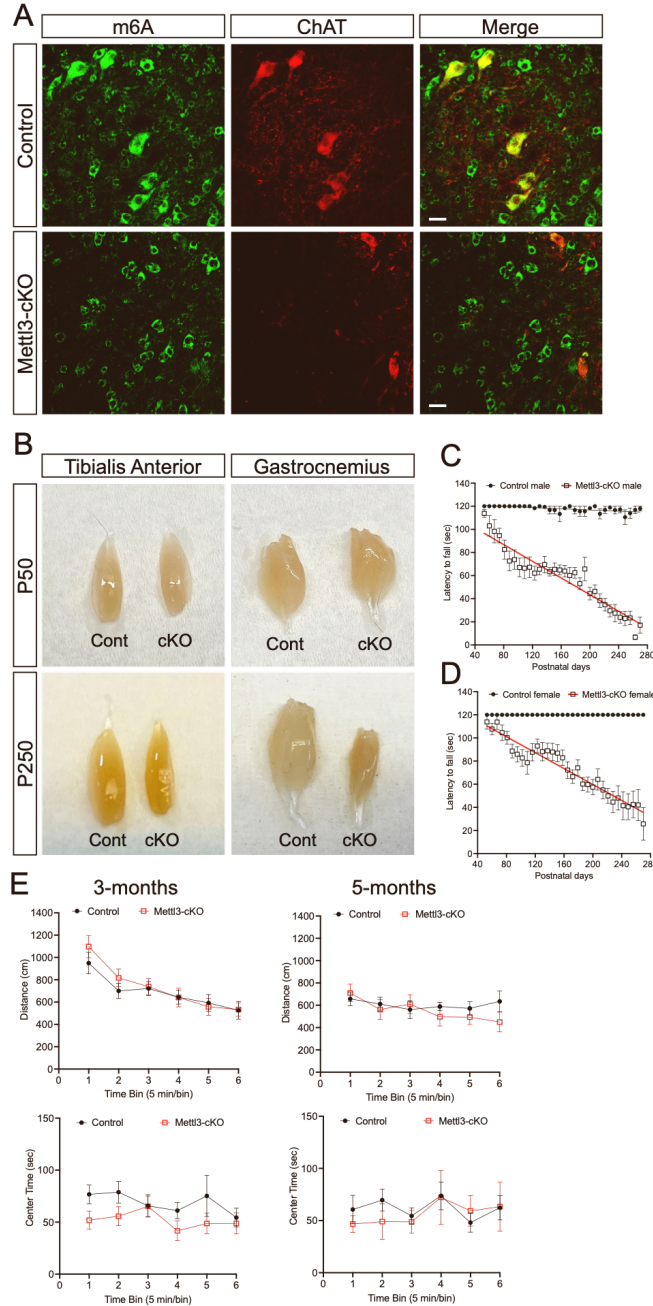
Figure S1. Morphological and behavioral analysis of *Mettl3*-cKO mice, related to Figure 1. (A) Spinal cords from eight-month-old control and *Mettl3*-cKO mice were stained with anti-m6A (green) and anti-ChAT (red) antibodies. Scale bar, 20 μM. (B) Representative images of TA and GC muscles from (P50, P250) *Mettl3* control (Cont) and *Mettl3*-cKO mice (cKO). (C) Inverted grid, males (n=9-12 / genotype). (D) Inverted grid, females (n=12-13 / genotype). For (B-C), data were analyzed by non-linear regression curve fit using the least sum-of-squares method, P<0.0001. (E) Open field at 3- and 5-months. The main effect of genotype is not significant for ambulatory distance: 3-months ($F_{1,17}$ =0.188, P=0.670); 5-months ($F_{1,17}$ =0.291, P=0.597), and for Center Time: 3-months ($F_{1,17}$ =2.504, P=0.132); 5-months ($F_{1,17}$ =0.116, P=0.738). Data were analyzed by Two-Way RM ANOVA.
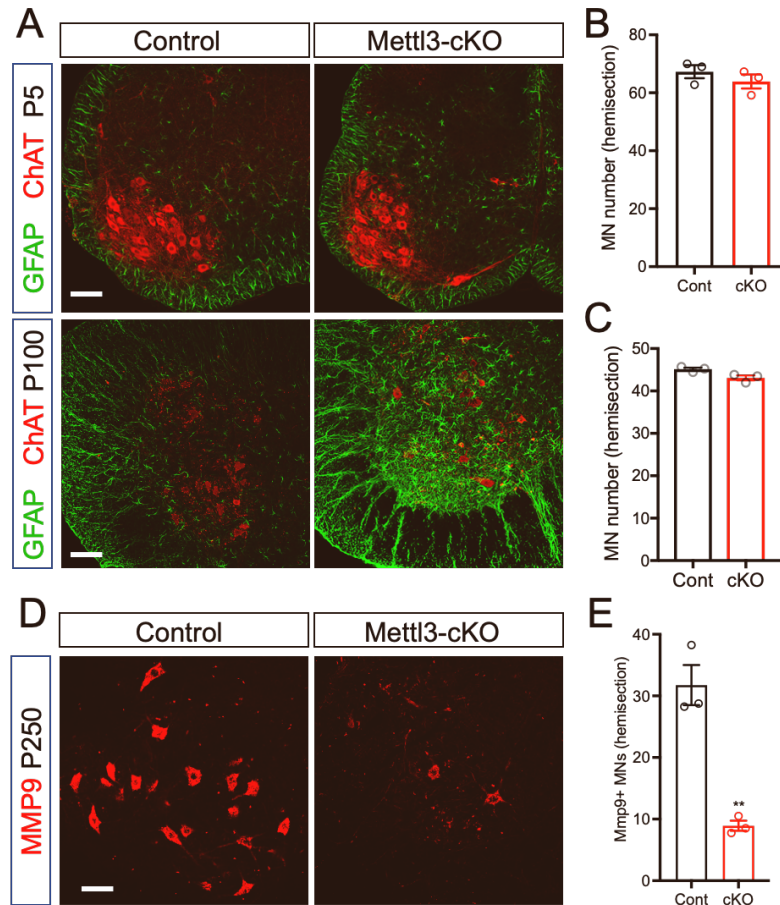
Figure S2. Analysis of motor neuron numbers and astrogliosis in *Mettl3*-cKO mice, related to Figure 2. (A) Immunostaining of ChAT (red) and GFAP (green) in ventral lumbar (L4-L5) spinal cords from P5 and P100 control and *Mettl3*-cKO mice. (B-C) Quantification of MN number per hemi-section at P5 (B, *ns*) and P100 (C, *ns*). Data are means ± SEM of 3 independent experiments. Scale bar, 50 µm (D) Immunostaining of MMP9 (red) in ventral lumbar (L4-L5) spinal cords from P250 control and *Mettl3*-cKO mice. Scale bar, 50 µm. (E) Quantification of MMP9+ cells per hemi-section at P250 (P=0.0024). Data are means ± SEM of n=3 independent experiments analyzed by unpaired t-test.
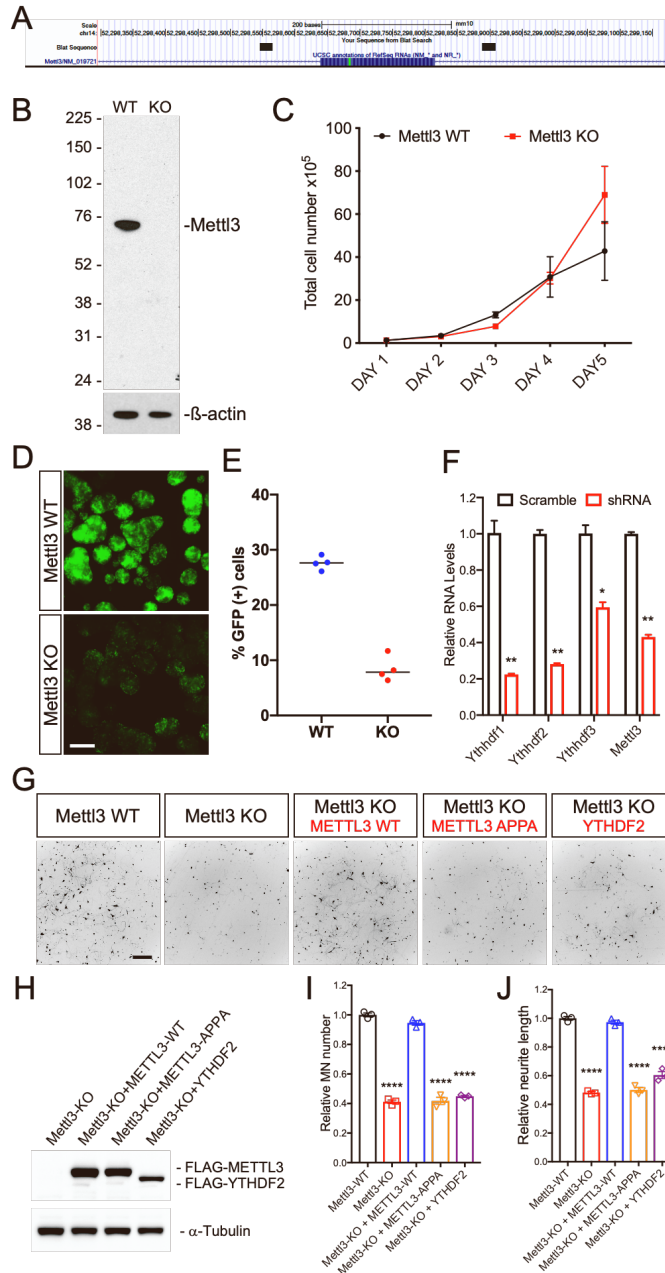
Figure S3. Validation of METTL3 KO and RNAi in ESCs, and rescue experiments with WT and catalytically inactive METTL3 in ES-MNs, related to Figure 3. (A) Schematic representation of exon 4 (blue box) and boundary 5' and 3' intronic regions (arrowed lines) of mouse *Mettl3* gene (UCSC browser; GRCm38/mm10; NM_019721), gRNAs target regions upstream and downstream of exon 4 (black boxes). (B) Western Blot of METTL3 from WT and *Mettl3*-KO mESCs. ß-actin was used as a loading control. (C) Proliferation assay of Mettl-WT and KO mESCs. (D) Live imaging of GFP-expressing ES-MNs (scale bar 500 μm) (E) Quantification of MN differentiation efficiency assessed by FACS analysis in ES-MNs. Data are means ± SEM of n=3 independent experiments analyzed by unpaired t-test (P<0.0001). (F) RT-

qPCR of ES-MNs transduced with LV-shRNA targeting *Ythdf1-3* and *Mettl3*. Data are means ± SEM of n=3 independent experiments analyzed by multiple paired t-tests (*Ythdf1*, P=0.0066; *Ythdf2*, P=0.0012; *Ythdf3*, P=0.0304; *Mettl3*, P=0.0016). (G) Fields of GFP-expressing WT or Mettl3-KO ES-MNs transduced with LVs expressing either FLAG-tagged WT or catalytically inactive (APPA) METTL3 and YTHDF2. Scale bar, 200 μm. (H) Western blot analysis using anti-FLAG antibody of total protein extracts from LV-transduced ES-MNs. (I-J) Quantification of normalized (relative to *Mettl3*-WT) mean number of ES-MNs (I) and neurite outgrowth (J). Data are means ± SEM of n = 3 independent experiments analyzed by one-way ANOVA with Tukey's post hoc test (adjusted P values in panel I: WT *vs.* KO p<0.0001; WT *vs.* KO + METTL3-WT p=0.1611; WT *vs.* KO + METTL3-APPA p<0.0001; WT *vs.* KO = YTHDF2 p<0.0001; adjusted P values in panel J: WT *vs.* KO p<0.0001; WT *vs.* KO + METTL3-WT p=0.7590; WT *vs.* KO + METTL3-APPA p<0.0001; WT *vs.* KO = YTHDF2 p<0.0001).
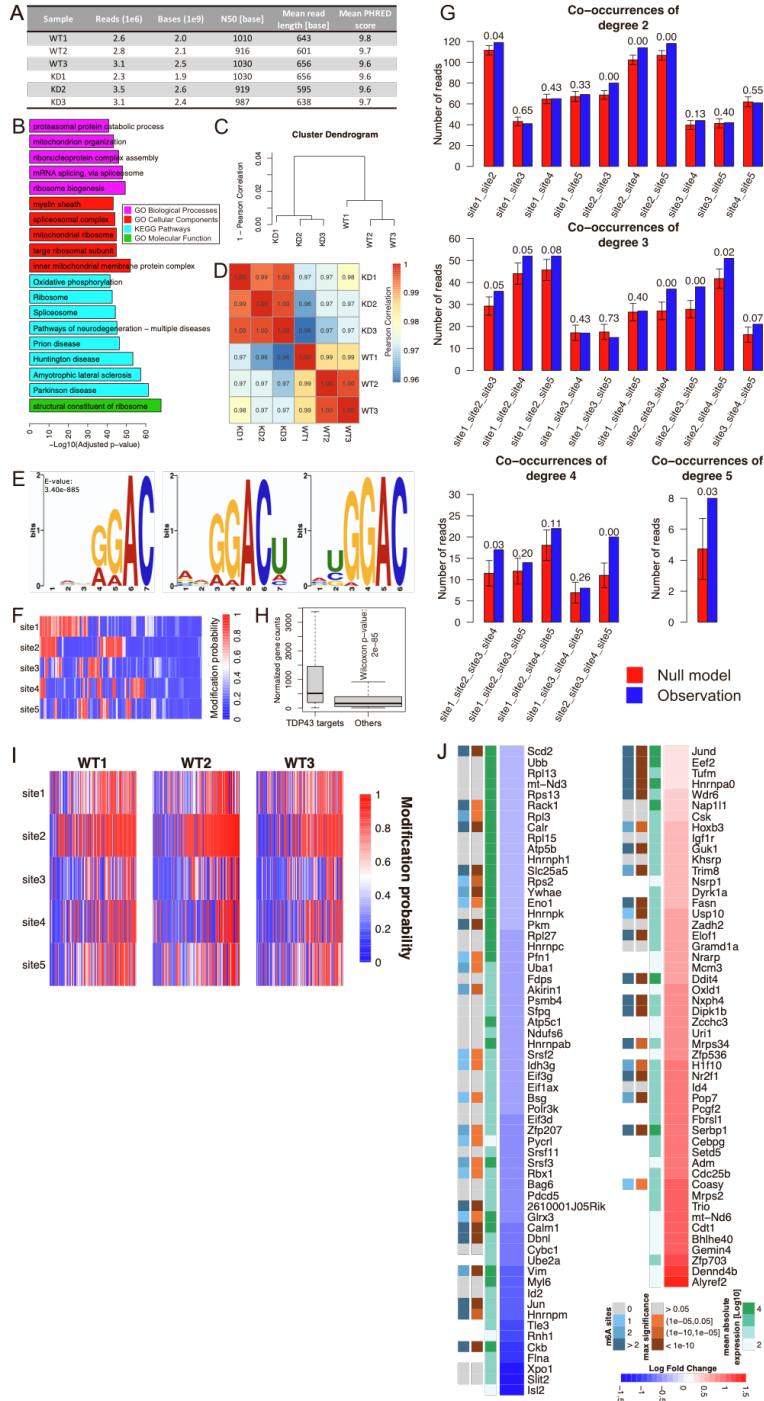
Figure S4. Nanopore-based direct RNA sequencing, related to Figure 4. (A) Metrics relevant to assess the quality of the sequencing runs. For each sample, we reported the name, number of sequenced reads, number of sequenced bases, N50 score, mean read length, and mean PHRED quality score. (B) Enrichment analyses for the genes tested by Nanocompore compared to all the transcriptional units annotated for mouse. The barplot shows highly significant terms (adjusted p-value <= 10e-40) from GeneOntology (GO Biological Processes, Cellular Components, and

Molecular Functions) and KEGG Pathways. (C) Hierarchical clustering of samples gene expression based on the correlation of DESeq2 normalized counts (26909 transcripts). (D) Pearson correlation matrix of DESeq2 normalized counts (26909 transcripts). (E) Motifs were detected in a window of 11 bases centered around the central nucleotide of each m6A+ 5-mer. The background for the enrichment test was constructed by randomly selecting 5000 5-mers from those analyzed by Nanocompore. (F) Heatmap showing the *Mettl3*-KO modification probability for each of the 5 TARDBP m6A sites (rows) in each read (columns). (G) The number of WT reads simultaneously modified for all the combinations of 2, 3, 4, and 5 sites (blue). In red, we reported the same quantity for a null model obtained by shuffling 1000 times the modification probabilities of each site (mean +/- 1 standard deviation). The number reported above each combination is the fraction of simulations with more co-occurrences than the WT counterpart. (H) Distributions of normalized gene count for TDP-43 targets (left) and other expressed genes (right). (I) Modification probability heatmap as in panel F stratified per sample. (J) Heatmap of the fold change (LogFC) of the differentially expressed TDP-43 targets reporting the number of m^6A sites, their maximum significance, and their mean absolute expression between WT and KO conditions.
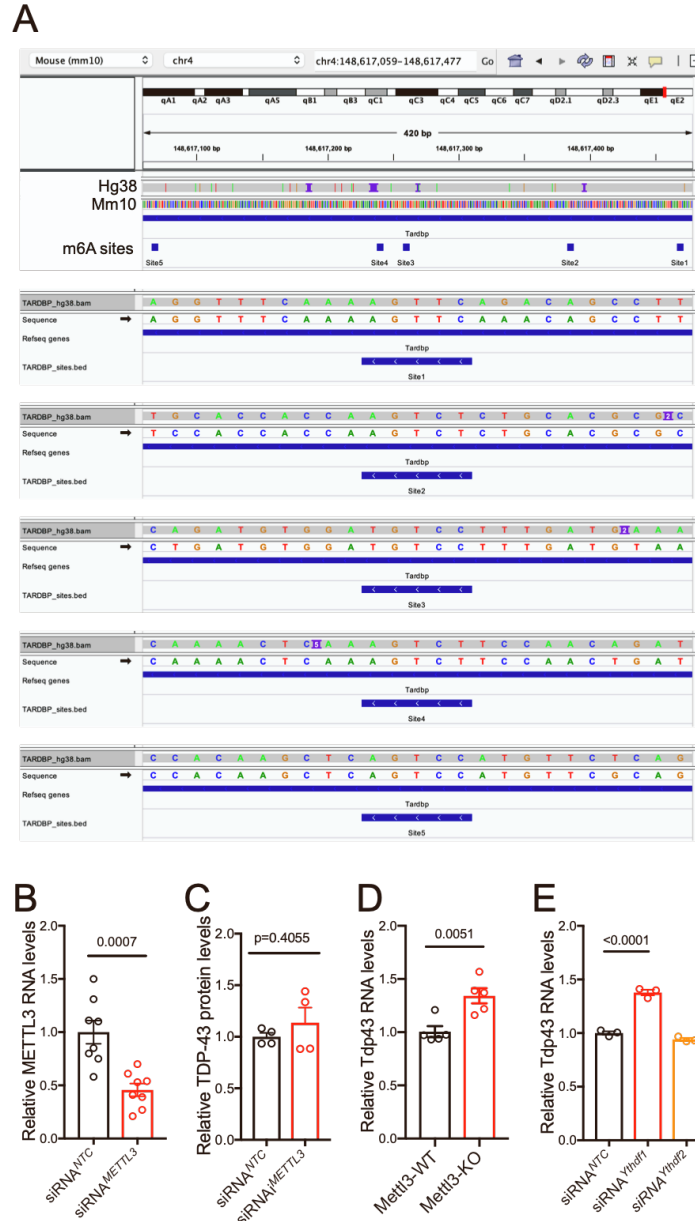
Figure S5. *TARDBP* m⁶A site conservation between human and mice and TDP-43 autoregulation analysis, related to Figure 5. (A) Alignment of mouse and human 3'UTR of TARDBP. (B) RT-qPCR of *METTL3* mRNA from HEK-293T cells transfected with siRNA^{NTC} or siRNA^{METTL3} (n=8, P=0.0007). (C) Quantification of TDP-43 protein levels in non-induced HEK293$^{HA-TDP-43}$ cells transfected with siRNA^{NTC} or siRNA^{METTL3} (n=4, P=0.4055). (D) RT-qPCR of endogenous mouse *Tardbp* mRNA from WT or *Mettl3*-KO ESMNs (n=5, P=0.0051). Data in C-D are means ± SEM of n≥4 independent experiments analyzed by unpaired t-test. (E) RT-qPCR of endogenous mouse TDP-43 mRNA from ES-MNs with *YTHDF1* and *YTHDF2* knockdown. Data are means ± SEM of n=3 independent experiments analyzed by one-way ANOVA with Tukey's post hoc test (adjusted P values: *YTHDF1*: P<0.0001; *YTHDF2*: P=0.1601).

Table S2. Primers and oligos used in this study.

RT-qPCR primers for mRNA levels

Name	Forward Sequence (5' to 3')	Reverse Sequence (5' to 3')
Mouse Hprt	TGGACTGATTATGGACAGGACTGAAAGA	GCCTCCCATCTCCTTCATGACATCT
Mouse Gapdh	AATGTGTCCGTCGTGGATCTGA	GATGCCTGCTTCACCACCTTCT
Mouse Mettl3	GGGAGGTAAGATCGGCTTACTG	CAGAGTAAACACCGGCCCTA
Human TARDBP	TGAACTGCTGTTTGCCTGATTG	GTGGGGTTCAAATTAAAACAAGGG
Human METTL3	AGCCTTCTGAACCAACAGTCC	CCGACCTCGAGAGCGAAAT
Human GAPDH	CTCAACGACCACTTTGTCAAGCTC	TCTTACTCCTTGGAGGCCATGT

PCR primers for genotyping

Name	Forward Sequence (5' to 3')	Reverse Sequence (5' to 3')
Mettl3 floxed	GTTGATGAAATTATCAGTACAATGGTTCTGA	GTAAAGAACAACTCTGGTTATCGTCATCG
ChAT-Cre WT	GTTTGCAGAAGCGGTGGG	GGCCACTTAGATAGATAATGAGGGGCTC
ChAT-Cre mut	TCGCCTTCTTGACGAGTTCTTCTG	GGCCACTTAGATAGATAATGAGGGGCTC

Guide RNA sequence and HDR oligo sequence for CRISPR/Cas9 deletion of *Mettl3*

Name	Sequence (5' to 3')
Mettl3 gRNA seq 1	TAATCACTTAATGTCTAATG
Mettl3 gRNA seq 2	TCATGCAGTAGCCATTCCAA
HDR oligo sequence	AGAAACCAGGCTCTTTGCATTTGAATTACATTCTAAATGCTTGTGAGGAGGACTGAGCCTATAACAACTCTGCTACATTGTTCATTCATATATTCCTCATGAATGGCTACTGCATGAGAAGGAGTACAGGCTCACTTGCAAGTAAAAGGAAGATTTTCTAGCCAAGCATCTGGATCTGAGTAACAATGAAAGTTAAAGTC

Sequence of siRNA and shRNA used for gene silencing

Name	Sequence (5' to 3')
Ythdf1 /TRCN0000348503	CCGGGGGTTGATTGTTGCATCTTTACTCGAGTAAAGATGCAACAATCAACCCTTTTTG
Ythdf2 /TRCN0000197932	CCGGGCAAACTTGCAGTTTATGTATCTCGAGATACATAAACTGCAAGTTTGCTTTTTTG
Ythdf3/ TRCN0000329408	CCGGCGTGTGGAGATGTCCTATTAACTCGAGTTAATAGGACATCTCCACACGTTTTTG